

PRMT1-methylated MSX1 phase separates to control palate development

Received: 19 October 2023

Accepted: 16 January 2025

Published online: 22 January 2025

 Check for updates

Li Meng^{1,2,7}, Yucheng Jiang^{1,7}, Jiawen You^{1,3}, Yatao Chen⁴, Shuyu Guo¹,
Liming Chen^{4,5}  & Junqing Ma^{1,6} 

Little is known about the regulation and function of phase separation in craniofacial developmental disorders. MSX1 mutations are associated with human cleft palate, the most common craniofacial birth defect. Here, we show that MSX1 phase separation is a vertebrate-conserved mechanism underlying embryonic palatal fusion. Notably, MSX1 phase separation is triggered by its intrinsically disordered protein region (IDR) and regulated by PRMT1-catalyzed methylation, specifically asymmetric dimethylation of arginine in the MSX1 IDR including R150 and R157. Hypomethylated MSX1 due to methylation site mutations and PRMT1 deficiency consistently leads to abnormal MSX1 phase separation to form less dynamic gel-like condensates, resulting in proliferation defects of embryonic palatal mesenchymal cells and cleft palate. Besides, high frequency mutations in the MSX1 IDR, especially R157S, have been identified in humans with cleft palate. Overall, we reveal the function and regulatory pathway of MSX1 phase separation as a conserved mechanism underlying cleft palate, providing a proof-of-concept example of a phenotype-associated phase separation mechanism associated with craniofacial developmental disorders.

Phase separation is thought to be a fundamental mechanism underlying many important biological processes, creating distinct physical and biochemical nonmembrane-bound compartments to regulate signaling, biochemical reactions, gene expression, and other processes^{1–5}. Phase separation is often triggered by intrinsically disordered regions (IDRs) in proteins^{6,7}. In addition to IDRs, posttranslational modifications (PTMs), including phosphorylation, methylation, ubiquitination, and sumoylation, have been reported to play important regulatory roles in phase separation⁸. The regulation of phase separation by PTMs is complex and not fully understood. The occurrence of less dynamic gel-like phase separation is an important

mechanism promoting human diseases, including neurodegeneration and cancer, and the possibility of directly targeting phase separation with several therapeutically plausible approaches has emerged^{4,9–11}. However, little is known about the regulation and function of phase separation in craniofacial development and disorders. Previous studies have identified many disease-associated mutations in craniofacial developmental disorders, including high-frequency mutations in protein IDRs¹². However, it is unclear whether and how mutations in protein IDRs, which lack a stable folded structure and are often annotated as proteins of unknown significance, contribute to the development of a genetic disorder.

¹State Key Laboratory Cultivation Base of Research, Prevention and Treatment for Oral Diseases, Nanjing Medical University, Nanjing, China. ²Department of Prosthodontics, Shanghai Ninth People's Hospital, Shanghai Jiao Tong University School of Medicine, College of Stomatology, Shanghai Jiao Tong University, National Center for Stomatology, National Clinical Research Center for Oral Diseases, Shanghai Key Laboratory of Stomatology, Shanghai Engineering Research Center of Advanced Dental Technology and Materials, Shanghai, China. ³Stomatological Hospital affiliated Suzhou Vocational Health College, Suzhou, China. ⁴Department of Biochemistry, School of Life Sciences, Nanjing Normal University, Nanjing, China. ⁵Jiangsu Cancer Hospital, Jiangsu Institute of Cancer Research, Affiliated Cancer Hospital of Nanjing Medical University, Nanjing, China. ⁶Department of Orthodontics, Affiliated Hospital of Stomatology, Nanjing Medical University, Nanjing, China. ⁷These authors contributed equally: Li Meng, Yucheng Jiang. ✉ e-mail: chenliming1981@u.nus.edu; chenliming1981@njnu.edu.cn; jma@njmu.edu.cn

Msh homeobox 1 (MSX1) plays an important role in craniofacial development, and mutations in MSX1 are associated with human cleft palate, the most common craniofacial birth defect in humans^{13–15}. Cleft palate, a complex genetic disorder, is caused by defective fusion between bilateral palatal shelves (two mesenchymal projections), where a defect in the proliferation of embryonic palatal mesenchymal cells (EPM) is a causative factor¹⁴. Msx1-deficient mice exhibit cleft palate, which results from an EPM proliferation defect^{14,15}. MSX1 contains an IDR at its N-terminus, but it is largely unknown whether and how IDR-containing MSX1 contributes to normal craniofacial development and cleft palate via a phase separation-associated mechanism.

Protein arginine methyltransferase 1 (PRMT1) is a key enzyme for protein arginine (R) dimethylation in vertebrates, and Prmt1-deficient mice exhibit cleft palate with reduced EPM proliferation, recapitulating the craniofacial developmental abnormalities observed in Msx1-deficient mice^{16,17}. R150 and R157 in the MSX1 IDR are the two potential methylation sites¹⁸. However, it remains to be determined whether and how PRMT1 directly methylates R150 and/or R157 in the MSX1 IDR to contribute to normal craniofacial development and cleft palate.

In this study, we demonstrated that MSX1 phase separation regulated by PRMT1-catalyzed methylation is one of the mechanisms underlying cleft palate in craniofacial development. MSX1 phase separation is triggered by its IDR and is precisely modulated by PRMT1-mediated R dimethylation, where PRMT1 directly binds MSX1 to dimethylate R150 and R157 in the MSX1 IDR. Defects in PRMT1-catalyzed MSX1 R150 and R157 dimethylation led to abnormal MSX1 phase separation, leading to the formation of less dynamic gel-like condensates, which caused EPM proliferation defects and cleft palate. The function and regulation of PRMT1-methylated MSX1 phase separation are conserved in vertebrates from zebrafish to humans and are clinically related to human cleft palate. Thus, this study provides a proof-of-concept example of a craniofacial developmental disorder as a phase separation-associated disease, which will be valuable for future innovations in preventative treatment and therapeutic approaches involving direct modulation of phase separation.

Results

MSX1 undergoes phase separation via an IDR at its N-terminus

The MSX1 protein consists of a DNA-binding domain (DBD) flanked by a repression domain (RD)-containing the N-terminal region and a subnuclear domain (SD)-containing the C-terminal region¹⁹. VL3 in PONDRA analysis revealed that the RD-containing N-terminal region in MSX1 is a largely unfolded IDR (Fig. 1A and Supplementary Fig. 1A)²⁰. Proteins with IDRs can undergo phase separation to form droplet-like condensates to mediate their biological functions⁶. These findings led us to investigate whether MSX1 with an IDR in its N-terminus can undergo phase separation. Indeed, immunofluorescence assays revealed that under physiological conditions, endogenous MSX1-formed circular droplet-like condensates uniformly distributed in the nucleus in human HEK293T cells, human EPM (HEPM), and mouse EPM (MEPM) (Fig. 1B, C and Supplementary Fig. 1B).

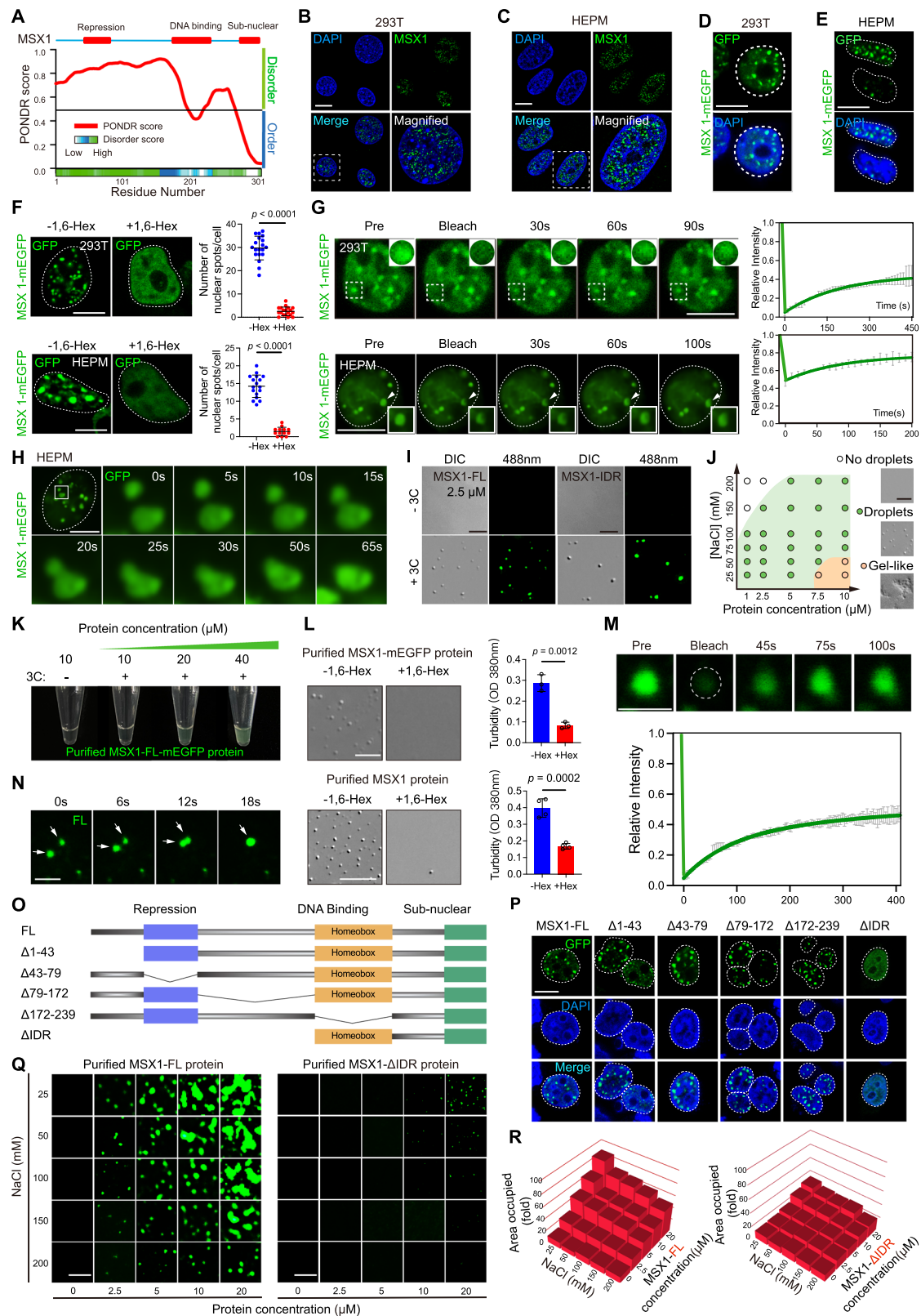
To explore the role of MSX1 phase separation during HEPM differentiation and palate development, we examined changes in MSX1 subnuclear localization during osteogenic differentiation and chondrogenic differentiation in cultured HEPM, and in mouse palate tissues from gestational day E13.5 to postnatal day P1, which encompasses the period of embryonic palate fusion²¹. Endogenous MSX1 similarly formed droplet-like condensates in the nucleus before and after induction of osteogenesis and chondrogenesis induction (Supplementary Fig. 1C, D). However, there were significantly more cells with MSX1 condensates at E14.5 than at other time points (Supplementary Fig. 1E, F). By E14.5 in mouse embryos, the palatal shelves have elevated to the horizontal position, make contact at the midline, and initiate fusion with each other, which is a critical period for EPM proliferation and palatal fusion²². These

findings indicate that dynamic MSX1 phase separation may play an important role in the spatiotemporal regulation of palatal fusion in mouse embryos. Consistent circular droplet-like condensates were observed in HEK293T and HEPM cells ectopically expressing the MSX1-mEGFP plasmid (Fig. 1D, E).

Previous studies have reported several membraneless organelles (MLOs) formed by the IDR-triggered protein phase separation in the nucleus, including nuclear speckles (NSs), promyelocytic leukemia protein (PML) nuclear bodies, and Cajal bodies, which contribute to the intracellular division of specific biological functions²³. We found that MSX1 droplet-like nuclear condensates did not colocalize with known nuclear MLOs, including PML bodies, NSs, and Cajal bodies (Supplementary Fig. 1G). Condensates formed by phase separation can be disrupted by 1,6-hexanediol (1,6-Hex)²⁴. In HEK293T and HEPM cells, droplet-like condensates formed by MSX1-mEGFP overexpression were disrupted by 1,6-Hex treatment (Fig. 1F). The ability to recover from photobleaching, as measured by fluorescence recovery after photobleaching (FRAP) assay, is an important physicochemical property of phase separation condensates²⁵. FRAP assays revealed that the fluorescence of MSX1-mEGFP droplets in HEK293T and HEPM cells recovered after photobleaching (Fig. 1G). Time-lapse photography of living cells revealed that MSX1-mEGFP droplets could fuse with each other (Fig. 1H). These results suggest that MSX1 droplet-like phase separation condensates in cells have a dynamic liquid-like nature.

To further investigate MSX1 phase separation in vitro, we purified MSX1 for in vitro phase separation assays (Supplementary Fig. 2A, B). In in vitro droplet formation assays, differential interference contrast (DIC) and fluorescence imaging revealed that purified MSX1 proteins formed droplets with a spherical shape (Fig. 1I). The results of the deletion of additional tags to exclude the influence of tags on the MSX1 protein were similar (Supplementary Fig. 2C–E). Overall, the abundance of MSX1 droplets increased with decreasing salt concentration and increasing protein concentration, whereas too low of a salt concentration and too high of a protein concentration led to gel-like protein aggregation (Fig. 1J and Supplementary Fig. 2F, G). A turbidity assay conducted by measuring the optical density (OD) of a protein solution at 380 nm is another approach adopted to quantify the capacity of protein phase separation²⁶. The results of the turbidity assay revealed that the turbidity of the MSX1 protein solution increased with increasing protein concentration (Fig. 1K and Supplementary Fig. 2H). Furthermore, different pH values and temperatures affected in vitro MSX1 droplet formation. Specifically, MSX1 phase separation peaked at pH = 6, and MSX1-formed aggregates tended to be gelatinous and solid with increasing temperature (Supplementary Fig. 2I–L). Consistent with MSX1 forming droplet-like condensates in cells via phase separation, droplets formed by the MSX1 protein in vitro were also disrupted by 1,6-Hex treatment and recovered after photobleaching with a half-recovery time ($t_{1/2}$) of 88.28 s (Fig. 1L, M). Furthermore, droplets formed by the MSX1 protein in vitro showed droplet fusion over time (Fig. 1N). These in vitro phase separation assays using purified MSX1 proteins confirmed that MSX1 can undergo phase separation to form droplet-like condensates with liquid-like dynamic properties.

We then investigated the role of the IDR and other domain regions in MSX1 phase separation by constructing a series of plasmids to produce different MSX1 mutants for phase separation assays in cells and in vitro (Fig. 1O). In cells overexpressing full-length wild-type MSX1 (MSX1-FL) or any of the MSX1 truncation mutants, fluorescence assays revealed that only Δ IDR, an MSX1 mutant lacking the IDR, presented severe defects in nuclear condensate formation, suggesting that the IDR of MSX1 is required for its droplet-like condensation in cells (Fig. 1P and Supplementary Fig. 2M). Furthermore, in vitro phase separation droplet formation assays using purified



proteins (Supplementary Fig. 3A), the Δ IDR protein had a reduced ability to form droplet-like condensates (Fig. 1Q, R and Supplementary Fig. 3B). Consistent with this, in vitro phase separation turbidity assays, the Δ IDR protein solution showed significantly reduced turbidity compared with the MSX1-FL protein solution (Supplementary Fig. 3C). Deletion of additional tags produced a similar result (Supplementary Fig. 3D, E). In in vitro droplet formation assays, DIC,

and fluorescence imaging revealed that the purified MSX1 IDR protein underwent phase separation to form droplets with a sphericity comparable to that of the MSX1-FL protein (Fig. 1I and Supplementary Fig. 2E). These results suggest that the IDR is required for MSX1 phase separation in cells and in vitro.

Taken together, our data demonstrate that MSX1 undergoes phase separation via its IDR.

Fig. 1 | MSX1 undergoes phase separation via an IDR at its N-terminus. **A** Order/disorder region prediction of MSX1 by the protein sequence and disorder prediction (PONDR) algorithm. **B**, **C** Representative immunofluorescence images for endogenous MSX1 in HEK293T (**B**) and HEPM (**C**). Scale bars, 10 μ m. **D**, **E** Representative confocal images of HEK293T (**D**) and HEPM (**E**) with ectopic overexpression of MSX1-mEGFP. Scale bars, 10 μ m. **F** Representative fluorescence images of MSX1-mEGFP expressing HEK293T and HEPM treated with dimethyl sulfoxide (DMSO) or 5% 1,6-Hex (left), and quantification of liquid droplets formed in the indicated cells. Scale bars, 10 μ m. HEK293T: n = 19. HEPM: -1,6-hex, n = 17; +1,6-hex, n = 13. **G** Representative graphs and quantitative analysis for the FRAP assay of MSX1-mEGFP condensates in HEK293T and HEPM. Scale bars, 10 μ m. n = 3 biologically independent experiments. **H** Time-lapse micrographs of MSX1-mEGFP droplet fusion in HEPM. Scale bars, 10 μ m. **I** Representative images of droplet formation of MSX1-FL-mEGFP and MSX1 IDR-mEGFP upon 3C cleavage. Scale bars, 10 μ m. **J** Phase diagram of MSX1-mEGFP at different protein concentrations as a function of salt concentration, achieved by scoring for the existence of droplets or

fibrillar hydrogels. Scale bars, 10 μ m. **K** Representative images for the turbidity assay of MSX1-mEGFP protein solution with increasing protein concentration. **L** Representative images and quantification of MSX1-mEGFP and MSX1 protein solution treated with DMSO or 5% 1, 6-Hex. Scale bars, 10 μ m. MSX1-mEGFP: n = 3, MSX1: n = 4 biologically independent experiments. **M** Representative droplet micrographs (top) and FRAP quantification (bottom) of MSX1-mEGFP protein in vitro. Scale bars, 10 μ m. n = 4 biologically independent experiments. **N** Time-lapse micrographs of MSX1-mEGFP droplet fusion in vitro. Scale bars, 5 μ m. **O** Schematic of MSX1 domains and truncated mutants. **P** Phase separation assay of truncated mutants of MSX1 in cells. Scale bars, 10 μ m. **Q** Representative images of droplet formation for MSX1-FL-mEGFP or MSX1- Δ IDR-mEGFP at different protein concentrations in 25–200 mM NaCl. Scale bars, 10 μ m. **R** Statistical analysis of the droplet formation of MSX1-FL-mEGFP or MSX1- Δ IDR-mEGFP. n = 3 biologically independent experiments. All data in this figure are represented as mean \pm SD from at least three biologically independent experiments with similar results. Two-tailed Student's t-test for (**F**, **L**). Source data are provided as a Source Data file.

PRMT1 regulates MSX1 phase separation by dimethylating MSX1

PRMT1, a key methyltransferase for protein R residue methylation, is an upstream regulator of MSX1 that regulates craniofacial development¹⁷. R methylation, an important PTM, has been shown to play important regulatory roles in protein phase separation and function^{27,28}. These findings led us to investigate whether and how PRMT1 modulates MSX1 phase separation through R methylation. Encouragingly, immunofluorescence assays revealed that inhibition of PRMT1 by its specific inhibitor MSO23 and depletion of PRMT1 by siRNAs caused significantly abnormal MSX1 phase separation by reducing the sphericity of the MSX1 condensates in the nucleus to form more gel-like condensates in cells than the controls (Fig. 2A, B and Supplementary Fig. 4A). FRAP assays confirmed that these more gel-like condensates were less dynamic, as evidenced by them requiring more time to reach half recovery (Fig. 2C–F).

As a key methyltransferase, PRMT1 is responsible for more than 90% of asymmetric arginine dimethylation (aDMA) events, rather than symmetric arginine dimethylation (sDMA) events²⁹. We found that PRMT1 interacts with MSX1, as evidenced by immunofluorescence assays showing the colocalization of endogenous MSX1 and PRMT1 in HEK293T and HEPM cell nuclei and reciprocal coimmunoprecipitation (Co-IP) analysis confirming the interaction between MSX1 and PRMT1 in cells, and pulldown assays using purified MSX1 and PRMT1 proteins confirming their direct interaction in vitro (Fig. 2G–I and Supplementary Fig. 4B). Immunofluorescence staining and Co-IP revealed that there was no significant change in the interaction between MSX1 and PRMT1 before and after the induction of osteogenic and chondrogenic differentiation (Supplementary Fig. 4C–E). Furthermore, cotransfection of MSX1-mEGFP and PRMT1-mCherry resulted in good colocalization of MSX1 with PRMT1 in the nucleus (Fig. 2J, K) and in vitro phase separation droplet formation assays revealed recruitment of PRMT1 into MSX1 droplets (Fig. 2L and Supplementary Fig. 4F). Furthermore, Co-IP analysis using methyl-arginine antibodies revealed that MSX1 undergoes aDMA rather than sDMA, and both the inhibition and depletion of PRMT1 decreased the aDMA levels of MSX1 (Fig. 2M, N). In vitro methylation assay results revealed that the purified MSX1 protein could be directly methylated by the purified PRMT1 protein via the use of S-adenosylmethionine (SAM) as a methyl donor (Fig. 2O).

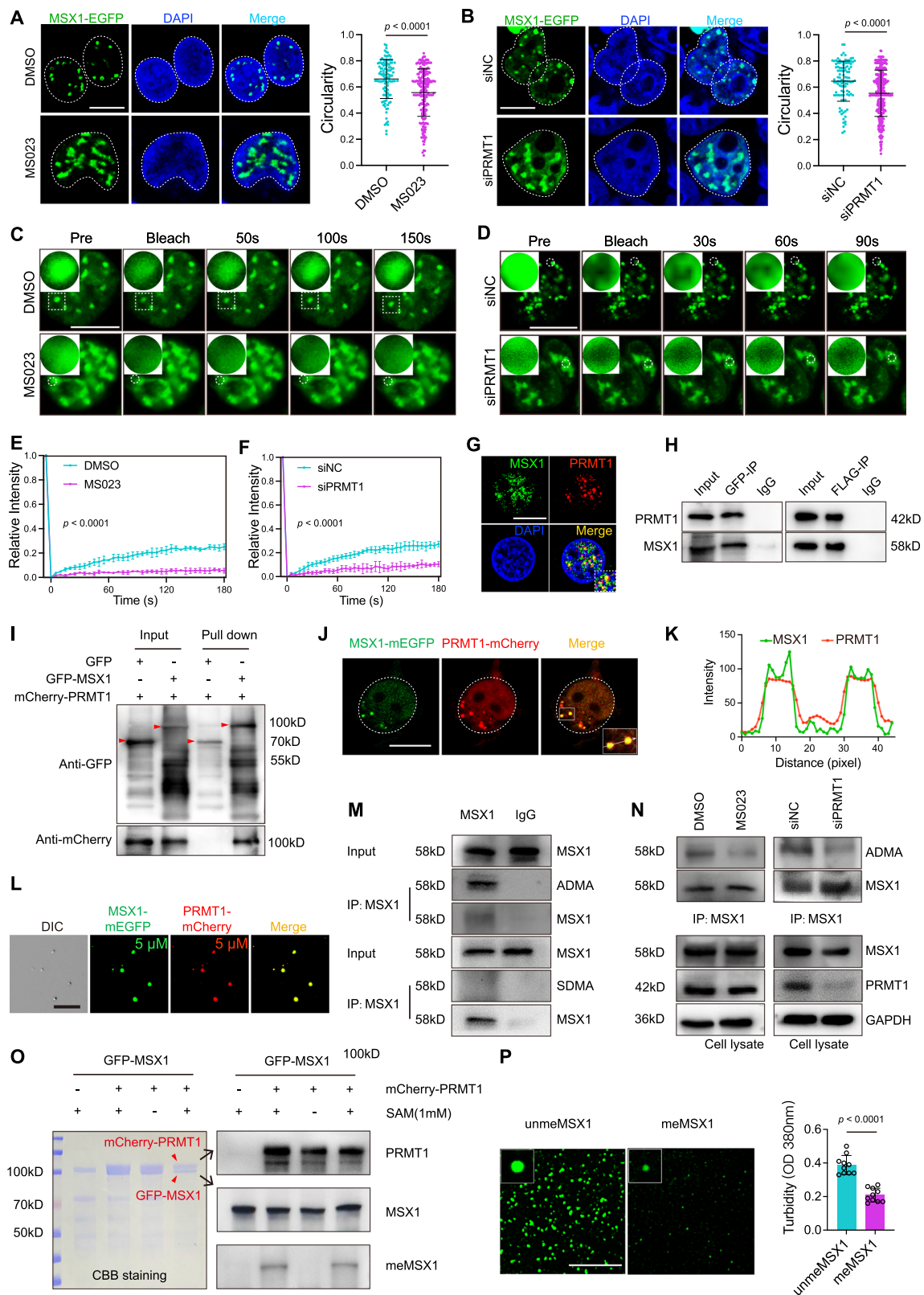
In in vitro phase separation droplet formation assays using purified proteins, the unmethylated MSX1 protein showed significantly altered phase separation compared with the PRMT1-methylated MSX1 proteins via an increased tendency to form condensates (Fig. 2P). These data suggest that PRMT1 regulates MSX1 phase separation by binding and aDMA-type demethylation of MSX1, with PRMT1-catalyzed MSX1 aDMA potentially important for the dynamic nature of MSX1 phase separation by reducing its tendency to condense into less dynamic gel-like condensates.

PRMT1 modulates MSX1 phase separation by methylating its IDR residues R150 and R157

We then sought to identify the specific R residues in MSX1 for PRMT1-catalyzed methylation. PTM prediction analysis using PhosphoSitePlus predicted R150 and R157 in the MSX1 IDR as the only two potential dimethylation sites, which was supported by mass spectrometry data¹⁸ (Fig. 3A). Co-IP analysis revealed that the R150S and R157S mutants both exhibited reduced binding to PRMT1, and their methylation levels were both lower than those of MSX1-FL (Supplementary Fig. 4G and Fig. 3B). Consistent with these findings, an in vitro methylation assay revealed that the R150S and R157S mutants showed strongly decreased PRMT1-catalyzed methylation (Fig. 3C). These results suggest that both R150 and R157 in the MSX1 IDR are methylation sites at which MSX1 is dimethylated by PRMT1.

We further investigated the role of PRMT1-catalyzed R150 and R157 methylation in MSX1 phase separation. In cells, immunofluorescence assays revealed that compared with MSX1-FL, both the R150S and R157S mutants formed more gel-like condensates with reduced sphericity in the nucleus (Fig. 3D, E). In support of these findings, these more gel-like condensates were less dynamic, recovered much less efficiently, and took longer to reach half recovery after photobleaching (Fig. 3F, G). The abnormal behavior of R150S and R157S phase separation is similar to that of MSX1 phase separation under the inhibition or depletion of PRMT1 as described above. Consistent with this, in vitro phase separation droplet formation assays using purified proteins, both the R150S and R157S proteins formed more gel-like condensates with reduced sphericity than MSX1-FL did (Fig. 3H, I). Deletion of additional tags produced a similar result (Supplementary Fig. 4H, I). These more gel-like condensates were less dynamic, as evidenced by the longer time to reach half recovery after photobleaching (Fig. 3J, K).

The R-to-S mutation might affect MSX1 phase separation by altering the MSX1 protein structure rather than the methylation level. To clarify whether the regulation of MSX1 phase separation by R150S and R157S mutations is methylation dependent, we mutated R150 and R157 to lysine (K) (an unmethylated mimetic) or phenylalanine (F) (a methylated mimetic)^{30–32}. R-to-K mutations are often used as unmethylated mimetics because they retain the positive charge of the arginine residue and eliminate its ability to be targeted by the arginine methyltransferase^{30,31}. In vivo and in vitro methylation assays confirmed that the methylation levels of the R150K, R157K, and R150/157K mutants were lower than those of MSX1-FL (Supplementary Fig. 4J, K). To further investigate whether MSX1 phase separation is affected by R150/R157-mediated methylation or protein conformation, we performed additional phase separation experiments using different R mutations. The R150S, R157S, R150K, and R157K mutants formed larger speckles in the nucleus than MSX1-FL and two other mutants, the



R150F and R157F mutants (Fig. 3L, M and Supplementary Fig. 4L, M). However, only the purified R150S and R157S proteins, but not the purified R150K, R157K, R150F, and R157F mutant proteins, significantly increased MSX1 protein aggregation in vitro (Fig. 3N, O and Supplementary Fig. 4N, O). The inconsistency of the R-to-K mutants and the consistency of R-to-F mutants between the in vivo (methylation) and in vitro (unmethylation) results suggested that the abnormal MSX1

phase separation was caused by demethylation rather than protein conformational changes caused by the R-to-S mutations.

Next, we overexpressed PRMT1 in R150S and R157S cells and observed that there was partial rescue of the circularity of MSX1 condensates after PRMT1 overexpression. The aberrant gel-like condensates caused by the R150S and R157S mutations tended towards droplet-like condensates, but they did not fully recover to the state

Fig. 2 | PRMT1 regulates MSX1 phase separation by dimethylating MSX1.

A Representative confocal images of MSX1-mEGFP-expressing HEK293T treated with DMSO or MS023 (left), and quantitative analysis of circularity (sphericity) of MSX1-mEGFP puncta per nucleus was shown (right). Scale bars, 10 μ m. DMSO: n = 115, MS023: n = 216 condensates. **B** Representative confocal images (left) and circularity quantification (right) of MSX1-mEGFP-expressing HEK293T transfected with NC siRNA or PRMT1 siRNA. Scale bars, 10 μ m. siNC: n = 105, siPRMT1: n = 310 condensates. **C** Representative images of FRAP of MSX1-mEGFP-expressing HEK293T treated with DMSO or MS023. Scale bars, 10 μ m. **D** Representative graphs of FRAP of MSX1-mEGFP-expressing HEK293T transfected with NC or PRMT1 siRNA. Scale bars, 10 μ m. **E** FRAP quantification of MSX1-mEGFP-expressing in HEK293T treated with DMSO or MS023. n = 3 biologically independent experiments. **F** Quantitative of FRAP assay in HEK293T transfected with NC or PRMT1 siRNA. n = 3 biologically independent experiments. **G** Representative immunofluorescence images for endogenous MSX1 and PRMT1 in HEK293T. Scale bars, 10 μ m. **H** Representative western blot images of reciprocal Co-IP analysis confirming the association between MSX1 and PRMT1 in HEK293T ectopically expressing MSX1-

mEGFP and PRMT1-FLAG. **I** Representative western blot images of pull-down assay using MSX1-mEGFP and PRMT1-mCherry purified proteins. **J**, **K** Confocal images (**J**) and colocalization analysis (**K**) of HEK293T with ectopic overexpression of MSX1-mEGFP and PRMT1-mCherry. Scale bars, 10 μ m. The white solid line indicates the nucleus. **L** Representative DIC and fluorescence images of condensates formed by purified proteins MSX1-mEGFP and PRMT1-mCherry. Scale bars, 10 μ m. **M** Representative western blot images of Co-IP assays assessing the aDMA and sDMA of MSX1. **N** Representative western blot images of Co-IP assays assessing the aDMA of MSX1 in treated with MS023 or PRMT1 siRNA. **O** Representative western blot images of in vitro methylation assay using MSX1 and PRMT1 purified proteins with/without S-adenosylmethionine (SAM) treatment. Coomassie blue-stained gel showed loading controls for MSX1 and PRMT1 purified proteins. **P** Droplet formation (left) and turbidity measurement (right) of unmethylated and methylated MSX1 purified proteins. Scale bars, 10 μ m. n = 10 samples. All data in this figure are represented as mean \pm SD from at least three biologically independent experiments with similar results. Two-tailed Student's t-test for (**A**, **B**, **E**, **F**, **P**). Source data are provided as a Source Data file.

observed before mutation (Fig. 3P, Q). As described above, compared with unmethylated MSX1, MSX1 methylated by PRMT1 tended to condense into less dynamic gel-like condensates. The gel-like condensates of the R150S and R157S proteins could be markedly reduced upon methylation by PRMT1, suggesting that both R150 and R157 in the MSX1 IDR, as PRMT1-targeted methylation sites, are important for MSX1 phase separation behavior (Fig. 3P–S and Supplementary Fig. 4P). These results further confirm the important role of the MSX1 IDR and its methylation by PRMT1 in the dynamic nature of normal MSX1 phase separation condensates.

Less dynamic gel-like MSX1 phase separation impairs EPM proliferation

Cell cycle-mediated EPM proliferation plays an important role in craniofacial developmental disorders¹⁶. To investigate the function of MSX1 phase separation in craniofacial developmental disorders, we first examined whether and how MSX1 phase separation is associated with the cell cycle and proliferation of EPM. In cell cycle assays using flow cytometry, the R150S and R157S MSX1 mutants, which exhibited less dynamic gel-like phase separation, resulted in a decreased proportion of S-phase cells with an increased proportion of G1-phase cells compared with MSX1-FL (Fig. 4A). PCNA, CCND1, CCNA2, and MKI67 are markers of cell proliferation^{33–35}. RT-qPCR analysis revealed that, compared with MSX1-FL, the R150S and R157S MSX1 mutants were significantly ineffective at increasing the expression of both the PCNA and CCND1 genes compared to MSX1-FL (Fig. 4B). The results of PCNA immunofluorescence staining were consistent, with the number of PCNA-positive cells among cells overexpressing the R150S and R157S MSX1 mutants being significantly lower than that among cells overexpressing MSX1-FL (Fig. 4C, D). These results suggest that the less dynamic MSX1 phase separation induced by R150S and R157S is associated with defects in EPM cell cycle progression and cell proliferation.

Furthermore, compared with MSX1-FL, PCNA immunofluorescence in HEPM with R-to-K and R-to-F mutants, which exhibit abnormal MSX1 phase separation, resulted in varying degrees of reduction in cell proliferation (Fig. 4C, D). Consistent with the methylation of R150 and R157 by PRMT1 attenuating MSX1 phase separation into proliferation-defective, less dynamic gel-like condensates, silencing PRMT1 decreased the proportion of S-phase cells with an increased proportion of G1-phase cells and reduced the number of PCNA-positive cells compared with those in the control (Fig. 4E–H).

MSX1 is a transcription factor³⁶. We performed transcriptomics analyses, including analysis of the quality of the transcriptome data and differentially expressed genes (DEGs) between normal MSX1 phase separation with MSX1-FL and abnormal MSX1 phase separation caused by R-to-S, R-to-F, and R-to-K mutations in HEPM

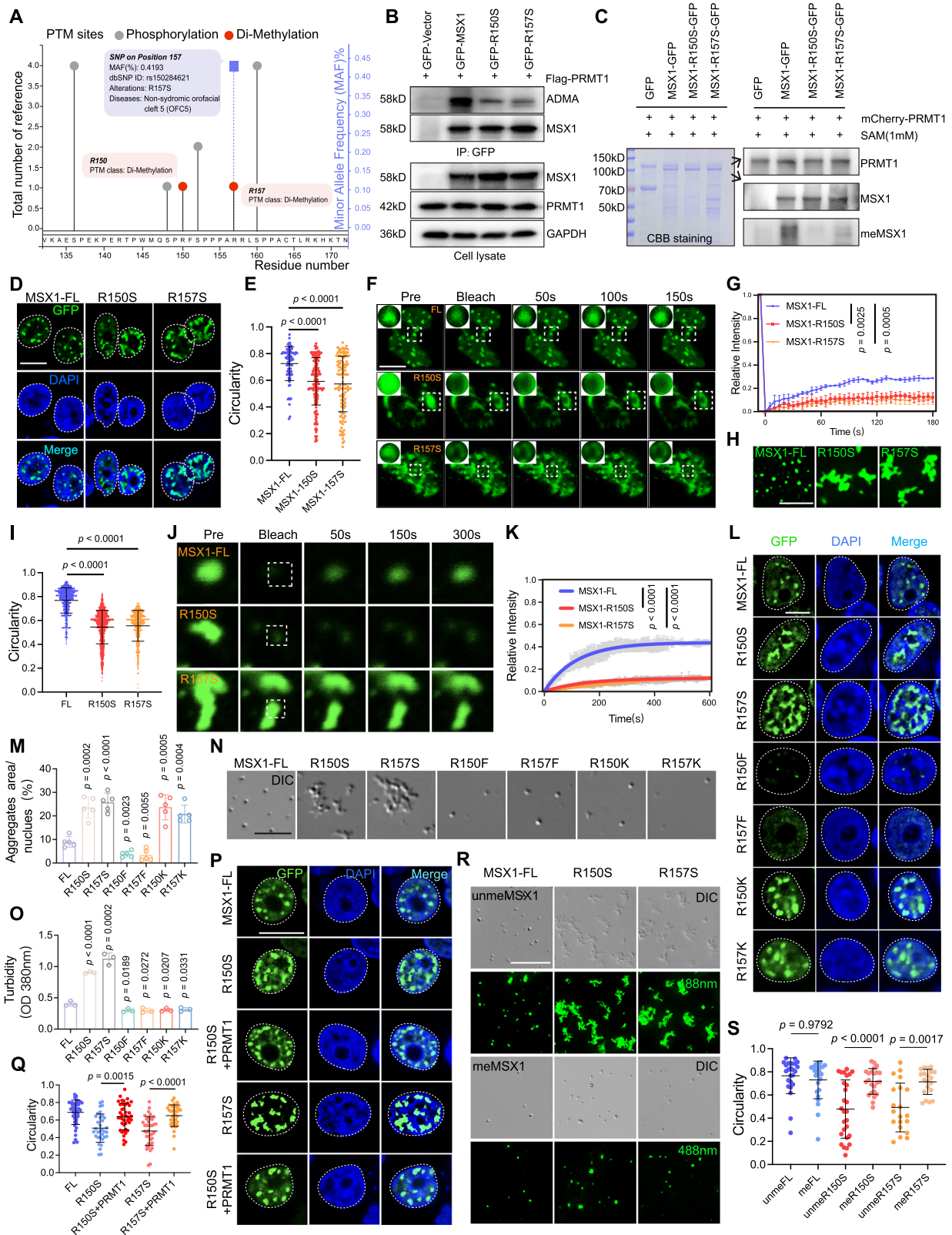
(Supplementary Fig. 5A–H and Supplementary Data 1). Although the DEGs between R157S_vs_FL, the DEGs between R157F_vs_FL, the DEGs between R157S_vs_FL, and the DEGs between R157K_vs_FL varied, the upregulated DEGs were consistently and significantly enriched in the regulation of cell proliferation (Supplementary Fig. 5I–K). These data suggest that mutations in the PRMT1-targeted methylation site in MSX1, resulting in abnormal MSX1 phase separation, might regulate HEPM cell proliferation through the transcriptional regulation of downstream genes. Tbx22 and Bmp4 are important downstream target genes of MSX1 in the regulation of palate development^{14,37}. We found that the promoter activities of Tbx22 and Bmp4 were reduced by MSX1 methylation site mutations (Supplementary Fig. 6A). The MSX1-CBP/P300 protein complex is crucial for MSX1 transcriptional activity³⁸, and Co-IP results revealed that there was no significant change in the level of the MSX1-CBP/P300 complex between MSX1-FL and its mutants, including R-to-S, R-to-F and R-to-K (Supplementary Fig. 6B).

To clarify whether the effect of MSX1 on HEPM cell proliferation is dependent on PRMT1, HEPM cells were cotransfected with MSX1-FL and PRMT1 siRNA. As shown in Fig. 4I–L, the increased cell proliferation induced by MSX1-FL was diminished by cotransfection with siPRMT1. These results indicate that PRMT1 plays a key role in the regulatory effect of MSX1 on HEPM cell function.

PRMT1 regulates several important signaling pathways in HEPM cell proliferation and palatal development, such as the BMP, TGF β , and WNT pathways¹⁶. Sonic hedgehog (SHH) and fibroblast growth factor (FGF) have been identified as essential components of signaling pathways for palatal development³⁹. We found that the SHH and FGF signaling pathways, as well as BMP, TGF β and WNT signaling pathways, were affected by PRMT1-regulated MSX1 methylation and methylation-mediated MSX1 phase separation (Supplementary Fig. 6C–E). The PRMT1 downstream pathway functions differently in different tissues during craniofacial development¹⁷. However, the regulatory mechanism of PRMT1-methylation-mediated MSX1 phase separation in the development of the calvaria was not exactly the same as that in the palate, which was partially applicable to other NCC-derived tissues in the craniofacial region (Supplementary Fig. 6F–K). It would be interesting to further investigate the regulatory mechanism of PRMT1-methylation-mediated MSX1 phase separation in the development of calvaria in the future. Nevertheless, these data suggest that MSX1 phase separation, which is regulated by PRMT1-mediated R150 and R157 methylation, underlies the regulation of HEPM proliferation and palate development.

Abnormal MSX1 phase separation underlies cleft palate

Defective EPM proliferation causes cleft palate, an abnormality of craniofacial development^{14–16}. As described above, abnormal PRMT1-



regulated MSX1 R150 and R157 methylation resulted in abnormal MSX1 phase separation, resulting in the formation of less dynamic gel-like condensates and proliferation defects in EPM. These findings led us to further investigate whether abnormal PRMT1-regulated MSX1 phase separation, which results in the formation of less dynamic gel-like condensates, can lead to cleft palate. PRMT1-catalyzed protein R dimethylation is conserved between mammals and nonmammals⁴⁰.

We found that PRMT1 is well conserved in vertebrates from zebrafish to humans (Supplementary Fig. 7). Although MSX1 IDRs are not well conserved between the nonmammal zebrafish and mammals, the human MSX1 R150 and R157 residues were found to be well conserved in vertebrates from zebrafish to humans (Fig. 5A and Supplementary Fig. 8). EPM are derived from neural crest cells (NCCs), and *Tg(sox10:egfp)* zebrafish are an established transgenic zebrafish line that

Fig. 3 | PRMT1 modulates MSX1 phase separation by methylating its IDR residues R150 and R157. **A** MSX1 PTM prediction. **B** Representative western blot images of aDMA-MSX1 levels in HEK293T transfected with indicated plasmids. **C** In vitro methylation assay of MSX1-FL/R150S/R157S-mEGFP purified proteins. **D–G** MSX1-FL-mEGFP, MSX1-R150S-mEGFP and MSX1-R157S-mEGFP phase separation in vivo. **D** Representative confocal images of condensates in HEK293T. Scale bars, 10 μ m. **E** Circularity quantification of condensates in HEK293T. MSX1-FL: n = 83, MSX1-150S: n = 187, MSX1-157S: n = 128 condensates. **F** FRAP analysis of MSX1 condensates in HEK293T. Scale bars, 10 μ m. **G** FRAP quantification of MSX1 condensates. n = 3 biologically independent experiments. **H–K** MSX1-FL-mEGFP, MSX1-R150S-mEGFP, and MSX1-R157S-mEGFP phase separation in vitro. **H** Representative confocal images of condensates formed by purified proteins. Scale bars, 10 μ m. **I** Circularity quantification of condensates formed by purified proteins. FL: n = 873, R150S: n = 1602, R157S: n = 773 condensates. **J** Representative images of FRAP assays assessing time-dependent fluorescence recovery of condensates formed by purified proteins. Scale bars, 1 μ m. **K** FRAP quantification of results condensates formed by purified proteins. n = 3 biologically independent experiments. **L–O** MSX1-FL-mEGFP, MSX1-R150S-mEGFP, MSX1-R157S-mEGFP, MSX1-R150F-mEGFP, MSX1-R157F-mEGFP, MSX1-R150K-mEGFP and MSX1-R157K-mEGFP phase separation in vivo and in vitro. **L** Representative confocal images of

HEPM expressing MSX1-FL-mEGFP or its mutants. Scale bars, 10 μ m. **M** Quantitative analysis of the area of MSX1-mEGFP puncta per nucleus. n = 5 fields. **N** Representative DIC images of condensates formed by purified proteins. Scale bars, 10 μ m. **O** Quantification of condensate turbidity using purified proteins. n = 3 biologically independent experiments. **P, Q** MSX1-FL-mEGFP, MSX1-R150S-mEGFP, MSX1-R150S-mEGFP+PRMT1, MSX1-R157S-mEGFP and MSX1-R157S-mEGFP+PRMT1 phase separation in vivo. **P** Representative confocal images in HEK293T. Scale bars, 10 μ m. **Q** Circularity quantification of condensates formed in HEK293T. FL: n = 44, R150S: n = 33, R150S + PRMT1: n = 43, R157S: n = 39, R157S + PRMT1: n = 36 condensates. **R, S** unmethylated or methylated MSX1-FL-mEGFP, MSX1-R150S-mEGFP, and MSX1-R157S-mEGFP phase separation in vitro. **R** Representative DIC and fluorescence images of condensates formed by purified proteins. Scale bars, 10 μ m. **S** Quantification of condensate sphericity using purified proteins. unmeFL: n = 25, meFL: n = 25, unmeR150S: n = 27, meR150S: n = 23, unmeR157S: n = 20, meR157S: n = 20 condensates. All data in this figure are represented as mean \pm SD from at least three biologically independent experiments with similar results. Two-tailed Student's t-test for (**M, O**), One-way ANOVA with Dunnett's multiple comparisons test for (**E, G, I, K**), One-way ANOVA with Turkey's multiple comparisons test for (**Q, S**). Source data are provided as a Source Data file.

expresses EGFP under the regulation of the *sox10* promoter for labeling NCCs and the ethmoid palate on the basis of EGFP fluorescence⁴¹. Therefore, we used *Tg (sox10: egfp)* zebrafish as our animal model to study the function and regulation of MSX1 phase separation in craniofacial development and cleft palate in vivo.

First, we generated *prmt1* MO zebrafish by injecting *Tg (sox10: egfp)* zebrafish embryos with antisense morpholino (MO) against *prmt1* to knock down *prmt1* in vivo (Supplementary Fig. 9A, B). The protein *phh3* is a marker of cell mitotic activity, and *phh3* positivity is associated with cell proliferation⁴². Consistent with the in vitro EPM cell proliferation results described above, *prmt1* MO zebrafish presented markedly fewer *egfp/phh3* double-positive cells than the *controls* did, suggesting that there were defects in EPM proliferation in vivo (Fig. 5B and Supplementary Fig. 9G, J). Compared with the *controls*, the *prmt1* MO zebrafish presented significantly greater rates of ethmoid palate defects (Fig. 5C and Supplementary Fig. 9H). Alcian blue staining of craniofacial cartilage confirmed that *prmt1* MO zebrafish presented a significantly greater rate of palate cleft than *control* zebrafish did (Fig. 5D, E and Supplementary Fig. 9C, I, K). Alterations in MSX1 aggregation in the cranial NCC migratory streams, which would develop into ethmoid palate, were detected in zebrafish embryos microinjected with *control* MO or *prmt1* MO at 12 h post-fertilization (*hpf*). Interestingly, a bright droplet-like speckle was visualized in the *control* group, whereas an irregular gel-like condensate was visualized in the *prmt1* MO group, revealing that MSX1 phase separation was also disrupted in palatal development of *prmt1* MO zebrafish embryos (Fig. 5F, G). We further generated *msx1* MO zebrafish by injecting *Tg (sox10: egfp)* zebrafish embryos with MO against *msx1* to knock down *msx1* in vivo (Supplementary Fig. 9D, E). Compared with the *control* zebrafish, *msx1* MO zebrafish also presented markedly fewer *EGFP/phh3* double-positive cells and a significantly higher palate cleft (Fig. 5H–L and Supplementary Fig. 9G–K). The Overexpression of PRMT1 only partially rescued the EPM proliferation defect and palate cleft in *msx1* MO zebrafish (Fig. 5H–L and Supplementary Fig. 9F–K). These results suggest that PRMT1 and MSX1 are functionally related and that both are important regulators of normal craniofacial development.

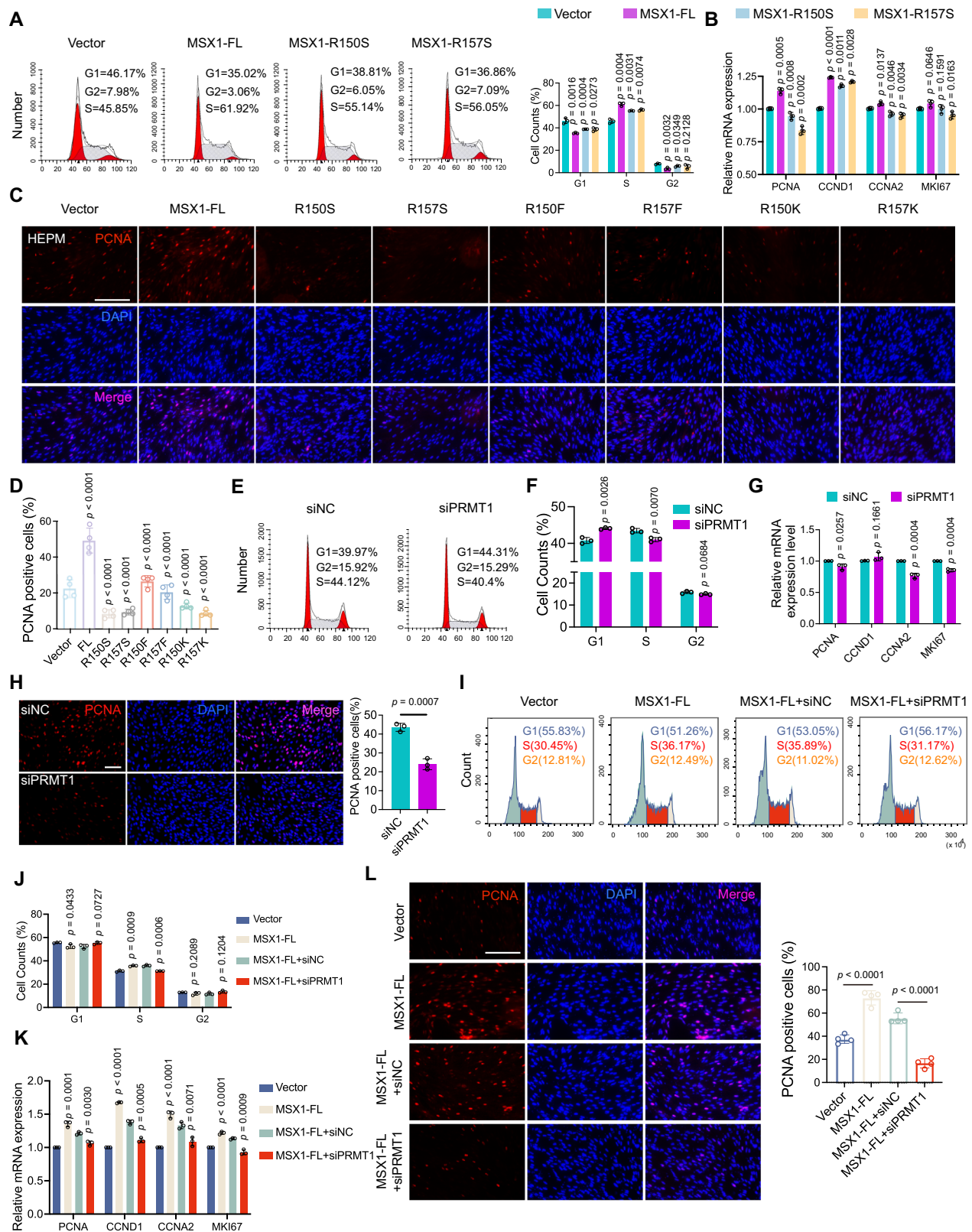
MSX1 phase separation is triggered by the IDR at its N-terminus. Accordingly, whether MSX1 with IDR deletion contributes to cleft palate via a phase separation-associated mechanism was investigated by microinjection of MSX1 Δ IDR mRNA into zebrafish. The reduction in EPM cell proliferation and cleft palate defects caused by *msx1* MO was rescued by MSX1-FL mRNA, but not by MSX1 Δ IDR mRNA (Supplementary Fig. 9L–P), demonstrating that MSX1 phase separation

disruption caused by IDR deletion hinders palate fusion by inhibiting cell proliferation in zebrafish embryos.

IDR- and PRMT1-mediated MSX1 methylation is critical for MSX1 phase separation to modulate HEPM cell proliferation in vitro. The R residues in the MSX1 IDR are conserved in vertebrates from zebrafish to humans, but whether PRMT1- and R residue-mediated MSX1 methylation is conserved in zebrafish is unknown. Co-IP analysis revealed a reduction in the methylated MSX1 level in *prmt1* MO and R-to-S mutant zebrafish embryos (Fig. 5M, N), suggesting that MSX1 methylation is conserved in zebrafish. Consistent with both R150 and R157 in the MSX1 IDR as the PRMT1-targeted methylation sites are important for the behaviors and functions of MSX1 phase separation, neither R150S nor R157S overexpression was as efficient as MSX1-FL overexpression in rescuing the EMP cell proliferation defects and preventing palate cleft in the *msx1* MO zebrafish (Fig. 5O–S and Supplementary Fig. 9G–K).

Although the palatogenic program is conserved from zebrafish to mammals⁴³, the obvious differences in craniofacial anatomy between zebrafish and humans present several limitations in research. To address this critique, we constructed PRMT1 and MSX1 knockdown mouse models by injection into pregnant mice with adenovirus carrying shPRMT1 or shMSX1 at E10.5 (Supplementary Fig. 10A, B and Supplementary Fig. 11A, B). Compared with those in the group injected with shControl adenovirus, embryos injected with shPRMT1 or shMSX1 presented a greater incidence of cleft palate (Supplementary Fig. 10C). Bilateral mesenchymal palatal shelves injected with shControl adenovirus arrived at the midline and converged with each other, whereas those in embryos injected with shPRMT1 and shMSX1 were smaller in size and failed to attach to each other (Supplementary Fig. 10D, F). Coinjection with adenovirus expressing MSX1-FL (AdFL) promoted palatal fusion and partially rescued the palate cleft caused by shMSX1, whereas R150S (AdR150S) and R157S (AdR157S) were not as effective as MSX1-FL in promoting palatal fusion (Supplementary Fig. 10B–D, F). Similarly, we tested MEPM cell proliferation in coronal sections and found that, compared with shControl, shPRMT1 and shMSX1 significantly reduced the fluorescence intensity of PCNA (Supplementary Fig. 10E, G), AdFL restored proliferation defects, whereas AdR150S and AdR157S were not as effective as MSX1-FL in restoring MEPM cell proliferation (Supplementary Fig. 10E, G).

Previous studies have reported that disruption of MSX1 and PRMT1 in the palatal mesenchyme leads to impaired proliferation of EPM and consequently to cleft palate in a cell type-specific conditional knockout mouse model^{17,37}. Our adenovirus mouse results are



consistent with those shown in the knockout mouse model (Supplementary Fig. 10, 11)^{17,37}. However, adenovirus injection into pregnant mice has limitations in knocking down genes in specific cell types compared with the conditional knockout mouse model. The functions and regulatory roles of MSX1 and PRMT1 in craniopharyngeal ectoderm-derived epithelial cells during palate development need to be further validated in the future via a conditional knockout mouse

model. Nevertheless, these findings indicate the high degree of conservation of the role of PRMT1-methylation-mediated MSX1 phase separation in EPM cell proliferation and palate development.

In human patients with MSX1 mutation-associated palate cleft, 86.57% of the mutations occurred in the IDR of MSX1, with R157S being a high-frequency pathogenic mutation (Supplementary Fig. 12A). Taken together, these data suggest that MSX1 phase separation

Fig. 4 | Less dynamic gel-like MSX1 phase separation impairs EPM proliferation. **A, B** HEPM ectopically expressing mEGFP-Vector, MSX-FL-mEGFP or its mutants, including R150S and R157S. **A** Flow cytometry assessing the cell cycle of HEPM. $n = 3$ biologically independent experiments. **B** RT-qPCR assessing the expression of proliferation marker genes, including CCND1, CCNA2, PCNA, and MKI67, in HEPM. $n = 3$ biologically independent experiments. **C, D** HEPM ectopically expressing mEGFP-Vector, MSX-FL-mEGFP or its mutants, including R150S, R157S, R150F, R157F, R150K and R157K. **C** Representative immunofluorescence staining images of PCNA in HEPM. Scale bars, 200 μm . **D** Quantification of PCNA-positive cells in HEPM. $n = 4$ biologically independent experiments. **E–H** HEPM transfected with siNC and siPRMT1. **E** Flow cytometry assessing the cell cycle of HEPM. **F** Quantification of flow cytometry in HEPM. $n = 3$ biologically independent experiments. **G** RT-qPCR assessing the expression of proliferation marker genes, including CCND1, CCNA2, PCNA, and MKI67. $n = 3$ biologically independent experiments. **H** Representative immunofluorescence staining images and

quantification of PCNA in HEPM. Scale bars, 200 μm . $n = 3$ biologically independent experiments. **I–L** HEPM transfected with mEGFP-Vector, MSX-FL-mEGFP, MSX-FL-mEGFP+siNC, and MSX-FL-mEGFP+siPRMT1. **I** Flow cytometry assessing the cell cycle of HEPM. **J** Quantification of flow cytometry in HEPM. $n = 3$ biologically independent experiments. **K** RT-qPCR assessing the expression of proliferation marker genes, including CCND1, CCNA2, PCNA, and MKI67. $n = 3$ biologically independent experiments. **L** Representative immunofluorescence staining images and quantification of PCNA in HEPM. Scale bars, 200 μm . $n = 4$ biologically independent experiments. All data in this figure are represented as mean \pm SD from at least three biologically independent experiments with similar results. Two-tailed Student's *t*-test for (**F–H**), One-way ANOVA with Dunnett's multiple comparisons test for (**A, B, D**), and Turkey's multiple comparisons test for (**J–L**). All data are representative of at least three independent experiments. Source data are provided as a Source Data file.

regulated by PRMT1-catalyzed methylation is a conserved important mechanism underlying normal craniofacial development and palate cleft.

Discussion

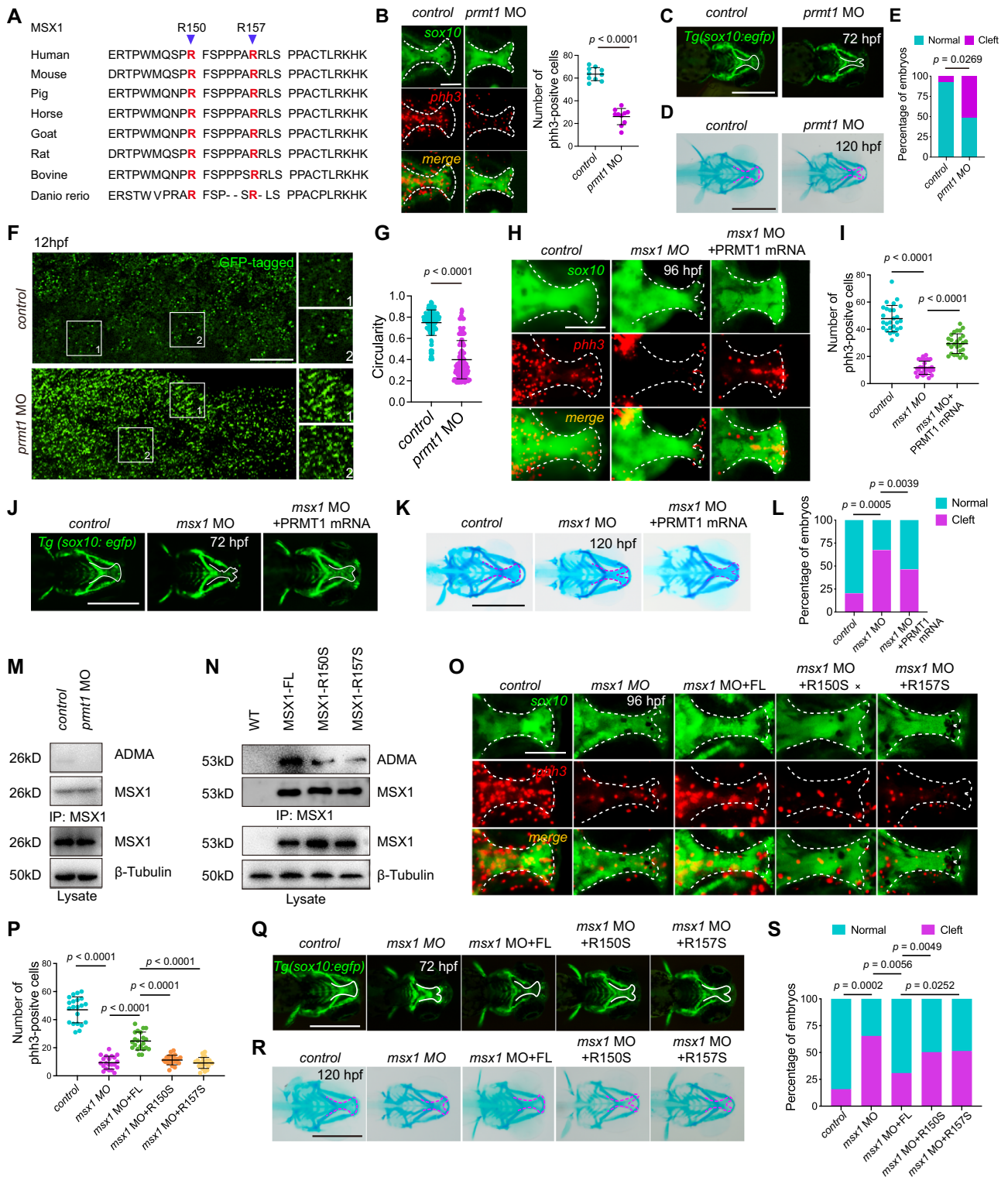
Phase separation, often triggered by IDRs in proteins, can drive the formation of nonmembrane organelles in cells to perform important biological functions in a context-dependent manner^{6,44}. MSX1 is a transcription factor³⁶. We found that the IDR of MSX1 induces the formation of droplet-like granules in the nucleus through phase separation. This finding is consistent with recent reports showing that several transcription factors, such as Pros, NELF, and CEBPA, undergo IDR-mediated phase separation^{45–47}. The dynamics of phase-separated compartments formed by proteins with IDRs can be positively or negatively regulated by PTMs, among which R methylation can weaken the R cation- π interactions to reduce the phase separation of FUS²⁸. Here, we showed that MSX1 phase separation, triggered by its IDR, is negatively regulated by R methylation, with defects in MSX1 R methylation resulting in less dynamic gel-like phase separation. Thus, MSX1 phase separation is spontaneously triggered by the MSX1 IDR, and R methylation on MSX1 lowers the threshold of MSX1 for condensation into less dynamic gel-like granules. Aberrant phase separation leading to less dynamic gel-like granules has been linked to the aberrant function of proteins in the granules and to human diseases, including neurodegeneration and cancer⁴⁸. We showed that the hypomethylation-induced less dynamic gel-like MSX1 phase-separated compartments recapitulated the abnormalities observed upon the loss of MSX1, including defects in EPM proliferation and cleft palate. Thus, IDR and R methylation likely coordinate to ensure that the dynamics of MSX1 phase-separated compartments function as required for MSX1 to carry out its biological functions.

Protein R methylation, IDR-mediated phase separation, and R methylation-regulated phase separation have all been shown to be important for protein biological functions^{6,27,49}. Our data showed that the IDR and its R methylation are linked to the regulation of the phase separation of MSX1, with PRMT-catalyzed methylation of the N-terminal IDR of MSX1. In particular, R150 and R157 in the IDR are mechanistically linked to a critical role in the phase separation of MSX1. Our studies are consistent with previous reports showing that R methylation on IDRs can regulate the phase separation of proteins, such as R methylation on the FUS IDR, which regulates the phase separation of FUS, and R methylation on the Ddx4 IDR, which modulates the phase separation of Ddx4^{27,28,50}. One perspective is that a single amino acid change in an IDR can perturb the threshold concentration for phase separation and may also change the material properties of condensates, ranging from dynamic liquids to aberrant less dynamic gel-like fibrils⁵¹. We showed that a single R150 or R157 amino acid change in the MSX1 IDR can reduce the dynamic nature of MSX1 phase-separated condensates and reduce the PRMT1-catalyzed R

methylation levels of MSX1. R cation- π interactions, which are weakened upon methylation, have been reported to be responsible for driving the phase separation and droplet formation of RG/RG-rich sequences found in the IDRs of FUS and Ddx4^{28,50}. These results suggest that both R150 and R157 in the MSX1 IDR, as the specific amino acids to be methylated by PRMT1, critically contribute to the phase separation of MSX1 and that PRMT1 regulates the phase separation of MSX1, possibly by methylating R150 and R157 to weaken R (cation- π) interactions.

Nonsyndromic cleft lip with or without palate (NSCL/P) is the most common craniofacial birth defect in humans, affecting approximately 1/700 live births worldwide¹³. The prevalence of nonsyndromic cleft palate (NSCP) is approximately half that of NSCL/P worldwide^{52,53}. Individuals with NSCP experience feeding difficulties as well as problems with breathing, speech, swallowing, and hearing, representing a substantial personal and societal burden⁵⁴. NSCP is considered a developmental disorder that may be triggered by genetic mutations⁵⁵. To date, the causative genes identified by genome-wide association studies (GWAS), along with candidate gene associations, linkage disequilibrium, and mutation detection, have included mainly IRF6, VAX1, MSX1, FOXE1, MYH9, MAFB, ABCA4, and BMP4⁵³. MSX1 mutations are found in 2% of human cleft palate cases⁵⁶. We found that most NSCP-associated MSX1 mutations (86.57%) occur in the N-terminal IDR of MSX1, with R157S in the IDR being one of the high-frequency NSCP mutations. The results obtained in *Msx1* knockout mice with cleft palate suggest an essential role of *Msx1* in normal palate development and cleft palate, but it is unclear whether and how NSCP-associated MSX1 IDR mutations, including the most prevalent mutations, act as genetic triggers for cleft palate. Our results revealed that the high frequency of the NSCP-associated R157S mutation, with a single amino acid change in the MSX1 IDR, is sufficient for the occurrence of cleft palate with EPM proliferation defects due to R157S phase separation into less dynamic gel-like condensates. This is because R157S cannot form methylated R157 by PRMT1, where R (cation- π) interactions and methylation-weakening R (cation- π) interactions are essential for MSX1 phase separation to form dynamic liquid-like condensates. These findings mechanistically explain previous findings showing that *Prmt1*-deficient mice develop cleft palates with reduced EPM proliferation and recapitulate the craniofacial developmental abnormalities observed in *Msx1*-deficient mice^{16,17}.

The regulation of craniofacial bone and structure by PRMT1-MSX1 is tissue specific, and the maxilla and palate of *Wnt1-Cre;Prmt1^{fl/fl}* mice are severely disrupted, while frontal bone formation is only moderately affected¹⁷. When MSX1 was overexpressed in different NCC-derived cell lines, the MSX1-FL protein was homogeneously and dispersedly distributed in the nucleus of MC3T3-E1 cells from the calvaria, which was completely different from droplet MSX1 phase separation in HEPM cells from the palate. Mutations of MSX1 methylation sites from R to S formed less dynamic gel-like condensates in EPM cells, while still



distributed dispersedly in MC3T3-E1 cells. Mutations of MSX1 methylation sites from R to F resulted in the formation of less and smaller spots in EPM cells, but they were still dispersed in MC3T3-E1 cells. However, mutations in MSX1 methylation sites from R to K resulted in larger speckles in both EPM and MC3T3-E1 cells than in MSX1-FL cells. These results revealed that MSX1 phase separation might be the reason why the palate and frontal bone are affected differently by PRMT1. MSX1 phase separation may regulate palatal development through signaling pathways such as BMP, SHH, and FGF, but the expression patterns and regulatory mechanisms of different signaling pathways

are specific to different craniofacial tissues^{57,58}, suggesting that the downstream effects of MSX1 phase separation are also different.

The majority of human proteins contain both folded protein domains and IDRs⁵⁹. GWAS has identified many mutations associated with human diseases, including both noncancer genetic disorders and cancers^{60,61}. Disease-associated mutations have been identified in both folded domains and IDRs^{48,62}. However, mutations in IDRs are often neglected or annotated as variants of unknown significance. PTMs including those involved in phosphorylation, arginine methylation, acetylation, and ubiquitination have been found to be key

Fig. 5 | Abnormal MSX1 phase separation underlies cleft palate. **A** Sequence alignment of MSX1 orthologs in indicated vertebrates assessing the conservation of the PRMT1 methylation sites. **B–G** *Control* MO and *prmt1* MO zebrafish embryos. **B** Representative images of *phh3* staining in zebrafish embryos (left) and quantification of *phh3*-positive cells in the ethmoid palate region of zebrafish embryos (right). Scale bars, 100 μ m. $n = 10$ embryos. The white dashed line indicates the ethmoid palate. **C** Representative fluorescence ventral views of zebrafish embryos. The white solid line indicates the ethmoid palate. Scale bars, 500 μ m. **D** Representative Alcian blue staining images of zebrafish embryos. The red dashed line indicates the ethmoid palate. Scale bars, 500 μ m. **E** Quantification of the cleft palate rates in zebrafish embryos. $n = 3$ biologically independent experiments. **F** Representative images of zebrafish embryos expressing GFP-tagged MSX1 at 12 hpf in the ethmoid palate region. Scale bars, 20 μ m. **G** Quantification of the circularity of MSX1 condensates in ethmoid palate region from zebrafish embryos. *control*: $n = 152$, *prmt1* MO: $n = 147$ condensates. **H–L** *Control* MO, *msx1* MO, and *msx1* MO + PRMT1 mRNA zebrafish embryos. **H** Immunofluorescence staining images of *phh3* in zebrafish embryos. The white dashed line indicates the ethmoid palate. Scale bars, 100 μ m. **I** Quantitative analysis of *phh3*-positive cells in the ethmoid palate region in zebrafish embryos. $n = 27$ embryos. **J** Fluorescence ventral views of zebrafish embryos. The white solid line indicates the ethmoid palate. Scale bars, 500 μ m. **K** Alcian blue staining images of zebrafish embryos. The red dashed

line indicates the ethmoid palate. Scale bars, 500 μ m. **L** Quantification of the cleft palate rates in zebrafish embryos. $n = 4$ biologically independent experiments. **M** Representative western blot images of aDMA-MSX1 levels in zebrafish embryos microinjected with *control* and *prmt1* MO. **N** Representative western blot images of aDMA-MSX1 levels in zebrafish embryos microinjected with MSX1-FL mRNA or its mutants, including R150S and R157S mRNA. **O–S** *Control* MO, *msx1* MO, *msx1* MO + FL mRNA, *msx1* MO + R150S mRNA, and *msx1* MO + R157S mRNA zebrafish embryos. **O** Representative immunofluorescence staining images of *phh3* staining of zebrafish embryos. The white dashed line indicates the ethmoid palate. Scale bars, 100 μ m. **P** Quantitative of *phh3*-positive cells in the ethmoid palate region in zebrafish embryos. $n = 21$ embryos. **Q** Representative fluorescence ventral views of zebrafish embryos. The white solid line indicates the ethmoid palate. Scale bars, 500 μ m. **R** Representative Alcian blue staining images of zebrafish embryos. The red dashed line represents the ethmoid palate. Scale bars, 500 μ m. **S** Quantification of the cleft palate rates in zebrafish embryos. $n = 3$ biologically independent experiments. MO: morpholino, hpf: hours post-fertilization. All data in this figure are represented as mean \pm SD from at least three biologically independent experiments with similar results. Two-tailed Student's t-test for (**B**, **E**, **G**, **S**), One-way ANOVA with Dunnett's multiple comparisons test for (**I**, **L**), and Turkey's multiple comparisons test for (**P**). Source data are provided as a Source Data file.

factors regulating phase separation through changes in the structure, charge, and hydrophobicity of the proteins involved in phase separation⁸. There is rapidly accumulating evidence that phase separation is an important principle for explaining the precise spatial and temporal regulation of normal development and that disease-associated mutations or PTMs alteration cause aberrant phase separation of proteins with IDRs and PTMs as disease-causing mechanisms. Several cancer-associated mutations have been reported to promote cancer development through aberrant phase separation with recently developed preventive and therapeutic drug candidates that target phase separation^{48,63}. There are no preventive or therapeutic drugs for cleft palate or many other noncancer developmental genetic disorders^{54,61,64,65}. By demonstrating MSX1 mutation-associated cleft palate as a proof-of-concept example, our study suggests that aberrant phase separation caused by mutations in IDRs can explain disease-associated mutations in noncancer developmental genetic disorders. Further exploration of the function and regulation of aberrant phase separation in developmental disorders is likely to provide promising potential targets for their prevention and treatment.

Methods

Ethics

The animal studies were reviewed and approved by the Ethics Committees of Nanjing Medical University (IACUC-2309039 for zebrafish, IACUC-2201021 for mice). All animal procedures were performed according to protocols and guidelines approved by the Animal Care Committee of Nanjing Medical University. Euthanasia of zebrafish and mice was performed according to the AVMA Guidelines for the Euthanasia of Animals.

Animals

Tg (sox10: egfp) zebrafish embryos were cultured on a 14 h/10 h light/dark cycle at 28.5 °C in Jiangsu Key Laboratory of Oral Diseases, Nanjing Medical University⁶⁶. Zebrafish were euthanized by rapid chilling (2–4 °C) until loss of orientation and cessation of opercular movements and then exposed for at least 20 additional minutes. Eight-week-old wild-type C57BL/6J mice were purchased from the Animal Experiment Center of Nanjing Medical University and maintained in the animal facility of Nanjing Medical University with a 12 h/12 h light/dark cycle at 22 °C under 40–60% relative humidity. Mice were given ad libitum access to food and water. Timed mating was established by the identification of vaginal plugs the morning following the housing

of a single male with multiple female mice. Noon of the day identifying vaginal plugs was considered as embryonic day 0.5 (E0.5). All mice were euthanized with an overdose of CO₂. All animals were used for analysis regardless of sex.

Antibodies

Primary antibodies used for immunoblotting were specific for anti-MSX1 (Bioss, bs-8512R, 1:1000), anti-GAPDH (Biorworld, APO063, 1:1000), anti-PRMT1 (Santa Cruz, sc-166963, 1:200), anti-ADMA (Cell signaling, 13522S, 1:1000), anti-SDMA (SAB, 30384, 1:1000), anti-GFP (Abbkine, ABT2020, 1:1000), anti-mCherry (abbkine, ABT2080, 1:1000), anti- β -tubulin (Affinity, T0023, 1:1000), anti-P-SMAD1 (Cell signaling, 13820, 1:1000), anti-P-SMAD2 (Cell signaling, 3108, 1:1000), anti-P-SMAD3 (Cell signaling, 9520, 1:1000), anti-SMAD1 (Cell signaling, 6944, 1:1000), anti-SMAD2 (Cell signaling, 5339, 1:1000), anti-SMAD3 (Cell signaling, 9523, 1:1000), anti-Active β -Catenin (Cell signaling, 19807, 1:1000), anti-AXIN2 (Abclonal, A2513, 1:1000), anti-P300 (Santa Cruz, sc-48343, 1:200), anti-SHH (Santa Cruz, sc-365112, 1:200), anti-GLII (Santa Cruz, sc-515751, 1:200), anti-FGFR1 (Santa Cruz, sc-57132, 1:200).

Primary antibodies used for Co-IP were specific for anti-MSX1 (Santa Cruz, sc-517256, 1:50), anti-FLAG (Abbkine, ABT2010, 1:250), anti-GFP (Abbkine, ABT2020, 1:250), anti-normal mouse IgG (Santa Cruz, sc-2025, 1:100), anti-normal rabbit IgG (Cell signaling, 2729, 1:250).

Primary antibodies used for immunofluorescence and immunohistochemistry staining were specific for anti-SC-35 (Abcam, ab11826, 1:50), anti-PML (Abcam, ab96051, 1:50), anti-Coilin (Abcam, ab11822, 1:50), anti-MSX1 (Bioss, bs-8512R, 1:50), anti-PRMT1 (Santa Cruz, sc-166963, 1:20), anti-GFP (Santa Cruz, sc-9996, 1:20), anti-PCNA (BOSTER, BMO104, 1:50), anti-PCNA (Proteintech, 60097-1-Ig, 1:50), anti-PHH3 (Santa Cruz, A2971, 1:20), anti-Vimentin (Cell signaling, 5741S, 1:50), anti-E-Cadherin (Cell signaling, 3195S, 1:1000), anti-Hexon (Bioss, bs-12354R, 1:50).

Morpholinos and mRNA microinjection

Morpholinos (MOs) and mRNA were injected into one-cell-staged zebrafish embryos using a micromanipulator (Nikon NARISHIGE, NT-88-V3). The following translation-blocking MO antisense oligonucleotides were obtained from Gene Tools (Philomath, USA): *msx1* MO, 5'-TAAAGCTCCGGTCTCAGAACATGC-3' (2 ng/embryo), *msx1* MO2, 5'-CCGGACTCGCTGAGCTTTTCAG-3' (2 ng/embryo), *prmt1* MO, 5'-TGCCGTCTCCGCATTTTCGATAAAC-3' (2 ng/embryo), *prmt1* MO2,

5'-ATTAGCATACACCCACCAGCCATTT-3' (2 ng/embryo) and standard control MO, 5'-CTAAAAGCA-GCAGGAGGCGATTCAT-3' (2 ng/embryo). The sequence of Human MSX1 and PRMT1 was obtained from the NCBI Gene Database. Then, the MSX1 full length, MSX1-R150S, MSX1-R157S, MSX1-mEGFP, and PRMT1 cDNA were cloned and ligated into the pXT7 vector at cloning sites EcoRI (GAATTC)-EcoRV(GATATC). Later, plasmids were linearized by BamHI and transcribed with the mMACHINE mMACHINE T7 kit (Ambion, AM1344). The capped mRNAs were injected into one-cell stage zebrafish embryos at 50 pg/embryo.

Fluorescence microscopy for zebrafish

Tg (sox10: egfp) zebrafish embryos at 72 hpf were anesthetized with 80–90 mg/L MS222 for 15 min and then photographed. *Tg (sox10: egfp)* zebrafish embryos at 96 hpf were euthanized and fixed in 4% paraformaldehyde (PFA) (Biosharp, BL539A). After dehydration and rehydration, the embryos were incubated with Proteinase K (10 mg/ml) (Sigma, 39450-01-6) for 10 min and re-fixed in 4% PFA for 20 min at room temperature (RT). After blocking, the embryos were stained with rabbit anti-*phh3* antibody and mouse anti-GFP primary antibody at 4 °C overnight. Alexa Fluor cy3 anti-rabbit (Beyotime, A0516) and Alexa Fluor 488 anti-mouse (Beyotime, A0428) were used as secondary antibodies. The images were captured using Zeiss LSM710 confocal microscopy with 488 nm and 594 nm laser lines (ZEN 2.3).

Cartilage staining

120 hpf zebrafish embryos were euthanized and fixed in 4% PFA overnight at 4 °C before staining with Alcian blue (Sigma, A5268) for cartilage. The samples were rinsed with 60:40 glycerol/1% KOH until they were sufficiently translucent and finally maintained in 100% glycerol. The judgment of cleft palate was through revealing a cleft in the ethmoid palate, where a population of cells in the median portion was absent^{67,68}.

Adenovirus production and injection

Adenoviruses were produced by Shanghai Genechem Co., Ltd. (MSX1: 5'-GCTGCTGCTATGACTTCTTTG-3'; PRMT1: 5'-GGACATGACATCCAAAGAC-3'; shCtrl: 5'-TTCTCCGAACGTGTACAGT-3'). MSX1-FL, MSX1-R150S, MSX1-R157S cDNAs from pmEGFP-N2-MSX1, pmEGFP-N2-R150S and pmEGFP-N2-R157S plasmids were cloned into GV314 vector. The sequences were listed in Supplementary Table 1. The adenovirus serotype used is adenovirus serotype 5 (Ad5). Pregnant mice were randomly divided and injected intraperitoneally with 200 μ L of suspensions including 2×10^9 plaque-forming units of adenovirus at E10.5.

Cells culture

Mouse embryonic palatal mesenchymal cells (MEPM) were isolated from embryonic palatal tissue in embryos of C57BL/6j mice at gestational day E13.5⁶⁹. In brief, mice were euthanized with CO₂ at E13.5. Paired palatal shelves were isolated and rinsed in PBS and subsequently in 100 μ L trypsin-EDTA (0.05%) (Thermo Fisher, 25300062) for 5 min at 37 °C with frequent agitation. Trypsinization was stopped by adding 1 mL of DMEM/F-12 medium (Gibco, C11330500BT) supplemented with 10% fetal bovine serum (FBS) (Vivacell, C04001-500) and 1% penicillin-streptomycin (PS) (Beyotime, C0222). MEPM were subsequently seeded on large dishes and cultured overnight at 37 °C. The next day, cells were washed with PBS, and fresh media was added. HEK293T (ATCC, CRL-11268), HEPM (ATCC, CRL-1486), and MC3T3-E1 (ATCC, CRL-2593) cell lines were obtained from the American Type Culture Collection. HEK293T cells were cultured in DMEM high glucose medium (Gibco, C11995500BT) and HEPM, MC3T3-E1 cells in α -MEM (Gibco, C12440500BT) supplemented with 10% FBS and 1% PS at 37 °C and 5% CO₂ in a humidified incubator. The culture medium was changed every three days. MS023 (MCE, HY-19615), or an equal volume

of DMSO (Sigma, BCCD8942) vehicle, was added to cells for 24 h at a final concentration of 30 nM.

Plasmids construction

The MSX1-mEGFP construct was generated by PCR and subcloned into the pmEGFP-N2 mutated by pEGFP-N2 (Clontech). MBP-MSX1-mEGFP construct was generated by PCR and subcloned into the pET-MBP-3C vector. Mutant MSX1-mEGFP containing various truncations and mutations in the MSX1 molecule were generated using PCR and similarly cloned into the above vectors. We initially designed primers to clone different regions of MSX1-FL (303 amino acids), Δ 1–43 (44–303), Δ 43–79 (1–44 + 80–303), Δ 79–172 (1–78 + 173–303), Δ 172–239 (1–171 + 240–303), Δ IDR (172–303), and IDR (1–172). The MSX1-R150S and MSX1-R157S were also generated by MSX1-FL using PCR cloning. The PRMT1-mCherry construct was generated by PCR and subcloned into the pmcherry-N2 vector, and the MBP-PRMT1-mCherry construct was subcloned into the pET-MBP-3C vector. The Flag-tag labeled PRMT1 construct was generated by PCR and subcloned into the p3xFlag-CMV vector. The primers were listed in Supplementary Table 1. Plasmids were extracted by transforming DH5 α (TIANGEN, CB101) with the corresponding plasmids and extracted using FastPure Plasmid Mini Kit (Vazyme, DC201) according to the manufacturer's protocol.

Transfection

Negative control siRNAs and siRNAs against PRMT1 were purchased from GenePharma (Shanghai, China). Cells at 70%–80% confluency were transiently transfected with plasmids and siRNAs using lipofectamine 2000 (Thermo Fisher, 11668019) and Opti-MEM (Thermo Fisher, 31985070) at a ratio of 1 μ g plasmid or siRNA to 1 μ L lipofectamine 2000 according to the manufacturer's instruction. Then cells were incubated for 8 h before refreshing the medium. The siRNAs sequences used are listed in Supplementary Table 2.

Quantitative real-time PCR (qRT-PCR)

Total RNA was isolated from cells, embryonic palate (E15.5), or zebrafish (48 hpf) using an RNA isolation kit (vazyme, RC101-01). RNA was reverse-transcribed into complementary deoxyribonucleic acid (cDNA) with HiScript III RT SuperMix (Vazyme, R323-01). Real-time PCR was conducted on the ABI-7300 Real-Time PCR System (Applied Biosystems) with ChamQ SYBR qPCR Master Mix (vazyme, Q341-02). Data were calculated using the $2^{-\Delta\Delta CT}$ method. The qPCR primers were listed in Supplementary Table 3.

Immunoprecipitation and Western blot

Cells, embryonic palate (E15.5) or zebrafish (48 hpf) were lysed with RIPA buffer (Beyotime, P0013B) containing 1 mM protease inhibitor PMSF (Beyotime, ST505) on ice for 30 min. The cell lysates were centrifuged at 10,010 $\times g$ for 15 min and the supernatants were incubated with Protein A+G Magnetic Beads (Beyotime, P2108) plus anti-MSX1 (Santa Cruz, sc-517256), PRMT1, GFP, FLAG or control IgG antibodies for at least 4 h at 4 °C. The beads were washed with phosphate-buffered saline containing Tween 20 (PBST) three times and the immunocomplexes were eluted into 5 \times SDS sample buffer by boiling for 5 min before western blot analysis. WB analysis was conducted with specific antibodies and secondary anti-mouse or anti-rabbit antibodies conjugated to horseradish peroxidase (HRP) (identified below). For protein samples of zebrafish embryos used for WB, we extracted proteins from fresh whole embryos. Specifically, 100/group zebrafish embryos were manually deyolked at 48 hpf and dissociated with lysis buffer, centrifuged at 4 °C for 15 min and the supernatant was boiled with 5 \times SDS sample buffer for 5 min as the embryonic extract, which was followed by WB analyses with antibodies. Visualization was achieved with chemiluminescence and

protein expression was quantified using ImageJ software. Uncropped and unprocessed scans of the blots are provided as a Source Data file.

Immunostaining and microscopy for mice and cells

Samples of mice for histological analysis were collected at E13.5, E14.5, E15.5, and P1 under the stereomicroscope. Embryonic head samples were fixed in 4% PFA for at least 24 h and then dehydrated, paraffin-embedded, sectioned at 5 μ m, and mounted on glass slides. Slice samples were rehydrated and antigen retrieval was performed with citrate buffer in a pressure cooker. Immunofluorescence and immunohistochemical staining were used to detect the phenotype differences and the expression of relevant molecules respectively. The degree of cleft palate severity *in vivo* was quantified by measuring the gap distance between the corresponding palatal shelves and the area of the palatal shelves from the photographs of H&E-stained sections using ImageJ program^{70,71}.

HEK293T, MEPM, HEPM, and MC3T3-E1 plated onto glass coverslips were transfected with plasmids or treated with various stimuli as indicated in the figures. Cells were then washed with PBS and fixed with 4% PFA for 30 min, permeabilized with 0.2% Triton X-100 for 20 min, and subsequently blocked with goat serum for 30 min at RT. Cells were then incubated with the appropriate primary antibodies (as indicated in the figures and listed in the “Antibodies” section) at 4 °C overnight, followed by staining with fluorescence-conjugated secondary antibodies for 1 h. The nuclei were counterstained with DAPI (Beyotime, C1005) for 3 min. Images were captured by Zeiss LSM710 confocal microscope system (ZEN 2.3 (blue edition)) using 63X NA APO lens or Leica DM 4000 microscope system (LAS X Life Science) with a 100 \times NA APO lens and analyzed with ImageJ, Zeiss confocal software (ZEN 2.3) and Leica Application Suite X software.

Cell cycle

The cell cycle of HEPM was evaluated by flow cytometry. In brief, HEPM were harvested with 0.05% trypsin-EDTA (Thermo Fisher, 25300062), washed by PBS two times, and further fixed in 70% ethanol at 4 °C for 18 h. Then, the cell cycle was detected by staining cells with propidium iodide (PI), followed by using the FACS Calibur flow cytometer (BD Biosciences, USA). The analysis was performed by FACS can cytometry (Becton-Dickinson, USA). All data were analyzed by Modfit LT 5.0.

Dual luciferase reporter assay

293T cells were cultured in 24-well plates at a density of 6.0×10^4 cells per well. When cells grew to 70%, they were cotransfected with pGL3-Promoter luciferase reporter vector containing the 5'-UTR fragment of BMP4 or TBX22, renilla vector (pRluc-TK) and plasmids over-expressing GFP or MSX1 or MSX1-R150S or MSX1-R157S or MSX1-R150F or MSX1-R157F or MSX1-R150K or MSX1-R157K using Lipofectamine 2000. 48 h after transfection, Luciferase activity was detected using the Dual Luciferase Reporter Assay System (Promega, Madison, WI, USA). The ratio of firefly luciferase activity to renilla luciferase activity was calculated for each sample.

Transcriptome sequencing

Total RNA was isolated from MSX1-FL, MSX1-R157S, MSX1-R157F, and MSX1-R157K cells using Trizol. The samples were then sent to Shanghai Majorbio Bio-Pharm Technology Co., Ltd for transcriptome sequencing. The sequencing data were analyzed on the online platform of Majorbio Cloud Platform (www.majorbio.com) and DEGs with *P* adjust value cutoff ≤ 0.05 and $|\log_2FC| > 1$ were considered to be significantly different.

Fluorescence recovery after photobleaching (FRAP)

FRAP assays were performed using the FRAP module of the Leica Stellaris STED and Zeiss LSM710 confocal microscopy system. For the *in vitro* FRAP experiment, spots of $\sim 2\text{-}\mu\text{m}$ diameter in $\sim 10\text{-}\mu\text{m}$ protein

droplets were photobleached with 20% laser power for 1 s using a 488-nm laser line. Time-lapse images were obtained within about a 2-min time course with a 1 s interval after bleaching. Cellular FRAP experiments were conducted at 37 °C in a live-cell imaging chamber. HEK293T and HEPM cells grown on glass bottom dishes were transfected with plasmids or treated with various stimulants as indicated in the figures until they reached the expected density. Target proteins were partially or fully photobleached with 20% laser power for 5 s using a 488-nm laser line. Post-bleach time-lapse images were collected over a 3-min time course after bleaching. For each experiment, the observed structure was bleached to approximately 50% of the initial intensity. Fluorescence intensities of regions of interest (ROIs) were measured using LAS X and ZEN 2.3 (blue edition) and corrected by unbleached control regions and subsequently normalized to pre-bleaching intensities of the ROIs. GraphPad Prism 8 was used to plot and analyze the FRAP results.

Recombinant protein expression and purification

Plasmids containing MBP and His-tagged genes were transformed into *E. coli* BL21 (DE3)-Rosetta cells (TIANGEN, CB108) and incubated in LB media with 100 mg/ml Ampicillin (Sangon Biotech, A610029) or Kanamycin (Sangon Biotech, A600286) at 37 °C at 180 rpm. When cells grew to OD 0.6–0.8, 0.1 mM IPTG (Yeason, 10902ES08) was added to induce protein expression, and the induction was maintained at 18 °C at 120 rpm for 18 h. Then, cells were ultrasonic split in lysis buffer (50 mM Tris-HCl, pH 7.5, 500 mM NaCl, 1 mM PMSF) at 80% of 300 W, on 5 s, off 10 s, remains 1.5 h. By supersonic spallation, the fusion protein is dissolved in lysate as a supernatant. These proteins were first purified using Ni-NTA Agarose (QIAGEN, 163026181), and then further purified using Superdex 200 Increase 10/300 GL with AKTA pure. These proteins were flash-frozen in liquid nitrogen, then stored in 150 mM Tris-HCl, pH 7.5, 500 mM NaCl, 1 mM DTT, and 10% glycerol at -80 °C. Purified proteins were examined by SDS-PAGE followed by Coomassie blue staining. Protein concentration was determined by BCA Protein Quantification Kit (Vazyme, E112-01) with Nanodrop measurement for OD 562 nm.

In vitro methylation

Methylation assays were conducted by dialyzing MSX1 and PRMT1 proteins against *in vitro* methylation buffer containing 50 mM Tris-HCl 1 mM EDTA, 1 mM DTT. 1 μ g recombinant MSX1 protein was methylated by incubating with 1 μ L S-adenosyl-L-methionine (SAM) (Yeason, 10619ES02) and 1 μ g recombinant PRMT1 protein at 30 °C for 2 h. 5 \times SDS protein loading buffer was added and heated at 95 °C for 10 min to stop reaction.

MSX1 droplet assay

Purified MBP-MSX1-mEGFP (FL, R150S or R157S) proteins were diluted in phase separation buffer (150 mM Tris-HCl, pH 7.5, 1 mM DTT) including a series of NaCl concentration (0–200 mM) and protein concentration (0–40 μ M) in a total volume of 50 μ L. MBP tag was cut by 3C Protease (Beyotime, P2302) at 4 °C overnight. Images of MSX1 droplets were performed by Zeiss LSM710 confocal microscopy using 63 \times magnification objective.

Quantification of cells with MSX1 granule clusters

For fixed cell quantification, HEK293T cells were initially fixed with 4% PFA for 30 min and then permeabilized with 0.2% Triton X-100 for 20 min at RT. Nuclear counter-staining was carried out using DAPI for 3 min. Images were captured by the Zeiss LSM710 confocal microscope system. For transient transfected cells, MS023 was added 24 h before fixation. At least three replicates of each experiment were conducted. A total of more than 150 cells were counted for each sample in order to quantify the percentage of cells with MSX1 puncta. Circularity quantification was performed through imageJ.

Circularity = $(4\pi \times \text{Area}) / (\text{Perimeter}^2)$ with a value of 1.0 indicating a perfect circle, while the value approaches 0.0, it indicates an increasingly elongated shape (for a circle, Area = πr^2 ; Perimeter = $2\pi r$).

Turbidity assay

Phase separation of MSX1 in the absence or presence of equimolar amounts was induced as described above for the droplet assay with various NaCl concentrations in a 20 μL total volume in a 384-well microplate. The absorption (turbidity) measurement was performed at 380 nm in a SpectraMax microplate reader. All experiments were performed in triplicate.

Pulldown assay

MSX1-mEGFP (FL/R150S/R157S) and PRMT1-mCherry proteins were separately expressed in DE3 cells and lysed by sonication and lysozyme treatment in lysis buffer. The cell lysates were then cleared by centrifugation at $21,000 \times g$ for 10 min and incubated with Anti-GFP Magnetic Beads (Sigma-Aldrich) at 4 °C overnight. Magnetic beads and their binding proteins were subsequently spun down, washed four times with lysis buffer, and boiled in $5 \times$ SDS sample buffer for 5 min.

Statistics and reproducibility

Samples were randomly divided into control and experimental groups and results are representative of a minimum of three biologically independent experiments with similar results expressed as mean \pm standard deviation (SD) unless stated otherwise. Statistical analyses were performed by GraphPad PRISM software (ver.8.3.0). The significance of differences between groups was assessed using two-tailed Student's *t*-tests, One-way ANOVA with Dunnett's multiple comparisons test, or One-way ANOVA with Turkey's multiple comparisons test. $P < 0.05$ was considered statistically significant.

Reporting summary

Further information on research design is available in the Nature Portfolio Reporting Summary linked to this article.

Data availability

The RNA-seq data generated in this study have been deposited in the Gene Expression Omnibus under accession code [GSE285740](https://www.ncbi.nlm.nih.gov/geo/query/acc.cgi?acc=GSE285740). The data generated in this study about reagents, primers, antibodies, generated plasmids, etc. are provided in the main text of this article and its Supplementary Information/Source Data file. Source data are provided with this paper.

References

- Boija, A. et al. Transcription factors activate genes through the phase-separation capacity of their activation domains. *Cell* **175**, 1842 (2018).
- Wang, S. et al. Targeting liquid-liquid phase separation of SARS-CoV-2 nucleocapsid protein promotes innate antiviral immunity by elevating MAVS activity. *Nat. Cell Biol.* **23**, 718–732 (2021).
- Xiao, Q., McAtee, C. K. & Su, X. Phase separation in immune signalling. *Nat. Rev. Immunol.* **22**, 188–199 (2022).
- Zhu, G. et al. Phase separation of disease-associated SHP2 mutants underlies MAPK hyperactivation. *Cell* **183**, 490–502.e418 (2020).
- Su, X. et al. Phase separation of signaling molecules promotes T cell receptor signal transduction. *Science* **352**, 595–599 (2016).
- Alberti, S., Gladfelter, A. & Mittag, T. Considerations and challenges in studying liquid-liquid phase separation and biomolecular condensates. *Cell* **176**, 419–434 (2019).
- Uversky, V. N. The multifaceted roles of intrinsic disorder in protein complexes. *FEBS Lett.* **589**, 2498–2506 (2015).
- Luo, Y. Y., Wu, J. J. & Li, Y. M. Regulation of liquid-liquid phase separation with focus on post-translational modifications. *Chem. Commun.* **57**, 13275–13287 (2021).
- Boyko, S. & Surewicz, W. K. Tau liquid-liquid phase separation in neurodegenerative diseases. *Trends Cell Biol.* **32**, 611–623 (2022).
- Zhang, J. et al. Myristoylation-mediated phase separation of EZH2 compartmentalizes STAT3 to promote lung cancer growth. *Cancer Lett.* **516**, 84–98 (2021).
- Zhang, S., Pei, G., Li, B., Li, P. & Lin, Y. Abnormal phase separation of biomacromolecules in human diseases. *Acta Biochim Biophys. Sin.* **55**, 1133–1152 (2023).
- Miyake, N. et al. Gain-of-function MN1 truncation variants cause a recognizable syndrome with craniofacial and brain abnormalities. *Am. J. Hum. Genet.* **106**, 13–25 (2020).
- Leslie, E. J. & Marazita, M. L. Genetics of cleft lip and cleft palate. *Am. J. Med Genet C. Semin. Med. Genet.* **163**, 246–258 (2013).
- Zhang, Z. et al. Rescue of cleft palate in *Msx1*-deficient mice by transgenic *Bmp4* reveals a network of BMP and Shh signaling in the regulation of mammalian palatogenesis. *Development* **129**, 4135–4146 (2002).
- Satokata, I. & Maas, R. *Msx1* deficient mice exhibit cleft palate and abnormalities of craniofacial and tooth development. *Nat. Genet.* **6**, 348–356 (1994).
- Gou, Y. et al. Protein arginine methyltransferase PRMT1 is essential for palatogenesis. *J. Dent. Res.* **97**, 1510–1518 (2018).
- Gou, Y. et al. Prmt1 regulates craniofacial bone formation upstream of *Msx1*. *Mech. Dev.* **152**, 13–20 (2018).
- Hornbeck, P. V. et al. PhosphoSitePlus, 2014: mutations, PTMs and recalibrations. *Nucleic Acids Res.* **43**, D512–520, (2015).
- Paysan-Lafosse, T. et al. InterPro in 2022. *Nucleic Acids Res.* **51**, D418–D427 (2023).
- Peng, K. et al. Optimizing long intrinsic disorder predictors with protein evolutionary information. *J. Bioinform. Comput. Biol.* **3**, 35–60 (2005).
- Hu, X., Gao, J., Liao, Y., Tang, S. & Lu, F. Retinoic acid alters the proliferation and survival of the epithelium and mesenchyme and suppresses Wnt/ β -catenin signaling in developing cleft palate. *Cell Death Dis.* **4**, e898 (2013).
- Bush, J. O. & Jiang, R. Palatogenesis: morphogenetic and molecular mechanisms of secondary palate development. *Development* **139**, 231–243 (2012).
- Hirose, T., Ninomiya, K., Nakagawa, S. & Yamazaki, T. A guide to membraneless organelles and their various roles in gene regulation. *Nat. Rev. Mol. Cell Biol.* **24**, 288–304 (2023).
- Wu, Y. et al. RNA-induced liquid phase separation of SARS-CoV-2 nucleocapsid protein facilitates NF- κ B hyper-activation and inflammation. *Signal Transduct. Target. Ther.* **6**, 167 (2021).
- Taylor, N. O., Wei, M. T., Stone, H. A. & Brangwynne, C. P. Quantifying dynamics in phase-separated condensates using fluorescence recovery after photobleaching. *Biophys. J.* **117**, 1285–1300 (2019).
- Huang, Y. et al. Common pitfalls and recommendations for using a turbidity assay to study protein phase separation. *Biochemistry* **60**, 2447–2456 (2021).
- Hofweber, M. et al. Phase separation of FUS is suppressed by its nuclear import receptor and arginine methylation. *Cell* **173**, 706–719.e713 (2018).
- Qamar, S. et al. FUS phase separation is modulated by a molecular chaperone and methylation of arginine cation- π interactions. *Cell* **173**, 720–734.e715 (2018).
- Wu, M. et al. Reduced asymmetric dimethylarginine accumulation through inhibition of the type I protein arginine methyltransferases promotes renal fibrosis in obstructed kidneys. *FASEB J.* **33**, 6948–6956 (2019).
- McBride, A. E. et al. Arginine methylation of yeast mRNA-binding protein Npl3 directly affects its function, nuclear export, and intranuclear protein interactions. *J. Biol. Chem.* **280**, 30888–30898 (2005).

31. Najbauer, J., Johnson, B. A., Young, A. L. & Aswad, D. W. Peptides with sequences similar to glycine, arginine-rich motifs in proteins interacting with RNA are efficiently recognized by methyltransferase(s) modifying arginine in numerous proteins. *J. Biol. Chem.* **268**, 10501–10509 (1993).
32. Campbell, M. et al. Protein arginine methyltransferase 1-directed methylation of Kaposi sarcoma-associated herpesvirus latency-associated nuclear antigen. *J. Biol. Chem.* **287**, 5806–5818 (2012).
33. Roa Fuentes, L. A., Bloemen, M., Carels, C. E., Wagener, F. A. & Von den Hoff, J. W. Retinoic acid effects on in vitro palatal fusion and WNT signaling. *Eur. J. Oral. Sci.* **130**, e12899 (2022).
34. Dong, S., Zhang, Y. & Huang, H. Involvement of RBP4 in all-trans retinoic acid induced cleft palate. *Mol. Med. Rep.* **16**, 5915–5923 (2017).
35. Song, Y. et al. FOXO1 regulates the formation of bovine fat by targeting CD36 and STEAP4. *Int. J. Biol. Macromol.* **248**, 126025 (2023).
36. Woloshin, P. et al. MSX1 inhibits myoD expression in fibroblast x 10T1/2 cell hybrids. *Cell* **82**, 611–620 (1995).
37. Zhu, S. et al. Essential role of Msx1 in regulating anterior-posterior patterning of the secondary palate in mice. *J. Genet. Genom.* **49**, 63–73 (2022).
38. Shetty, S., Takahashi, T., Matsui, H., Ayengar, R. & Raghov, R. Transcriptional autorepression of Msx1 gene is mediated by interactions of Msx1 protein with a multi-protein transcriptional complex containing TATA-binding protein, Sp1 and cAMP-response-element-binding protein-binding protein (CBP/p300). *Biochem. J.* **339**, 751–758 (1999).
39. Won, H. J., Kim, J. W., Won, H. S. & Shin, J. O. Gene regulatory networks and signaling pathways in palatogenesis and cleft palate: a comprehensive review. *Cells* <https://doi.org/10.3390/cells12151954> (2023).
40. Wang, Y. C. & Li, C. Evolutionarily conserved protein arginine methyltransferases in non-mammalian animal systems. *FEBS J.* **279**, 932–945 (2012).
41. Wada, N. et al. Hedgehog signaling is required for cranial neural crest morphogenesis and chondrogenesis at the midline in the zebrafish skull. *Development* **132**, 3977–3988 (2005).
42. Chen, L. T. et al. Functional and molecular features of the calmodulin-interacting protein IQCG required for haematopoiesis in zebrafish. *Nat. Commun.* **5**, 3811 (2014).
43. Swartz, M. E., Sheehan-Rooney, K., Dixon, M. J. & Eberhart, J. K. Examination of a palatogenic gene program in zebrafish. *Dev. Dyn.* **240**, 2204–2220 (2011).
44. Zhang, G., Wang, Z., Du, Z. & Zhang, H. mTOR regulates phase separation of PGL granules to modulate their autophagic degradation. *Cell* **174**, 1492–1506.e1422 (2018).
45. Liu, X. et al. Mitotic implantation of the transcription factor prospero via phase separation drives terminal neuronal differentiation. *Dev. Cell* **52**, 277–293.e278 (2020).
46. Rawat, P. et al. Stress-induced nuclear condensation of NELF drives transcriptional downregulation. *Mol. Cell* **81**, 1013–1026.e1011 (2021).
47. Christou-Kent, M. et al. CEBPA phase separation links transcriptional activity and 3D chromatin hubs. *Cell Rep.* **42**, 112897 (2023).
48. Tsang, B., Pritisanac, I., Scherer, S. W., Moses, A. M. & Forman-Kay, J. D. Phase separation as a missing mechanism for interpretation of disease mutations. *Cell* **183**, 1742–1756 (2020).
49. Guccione, E. & Richard, S. The regulation, functions and clinical relevance of arginine methylation. *Nat. Rev. Mol. Cell Biol.* **20**, 642–657 (2019).
50. Nott, T. J. et al. Phase transition of a disordered nuage protein generates environmentally responsive membraneless organelles. *Mol. Cell* **57**, 936–947 (2015).
51. Molliex, A. et al. Phase separation by low complexity domains promotes stress granule assembly and drives pathological fibrillization. *Cell* **163**, 123–133 (2015).
52. Jugessur, A., Farlie, P. G. & Kilpatrick, N. The genetics of isolated orofacial clefts: from genotypes to subphenotypes. *Oral. Dis.* **15**, 437–453 (2009).
53. Dixon, M. J., Marazita, M. L., Beaty, T. H. & Murray, J. C. Cleft lip and palate: understanding genetic and environmental influences. *Nat. Rev. Genet.* **12**, 167–178 (2011).
54. Wehby, G. L. & Cassell, C. H. The impact of orofacial clefts on quality of life and healthcare use and costs. *Oral. Dis.* **16**, 3–10 (2010).
55. Mangold, E., Ludwig, K. U. & Nothen, M. M. Breakthroughs in the genetics of orofacial clefting. *Trends Mol. Med.* **17**, 725–733 (2011).
56. Jezewski, P. A. et al. Complete sequencing shows a role for MSX1 in non-syndromic cleft lip and palate. *J. Med. Genet.* **40**, 399–407 (2003).
57. Hu, D. & Helms, J. A. The role of sonic hedgehog in normal and abnormal craniofacial morphogenesis. *Development* **126**, 4873–4884 (1999).
58. Graf, D., Malik, Z., Hayano, S. & Mishina, Y. Common mechanisms in development and disease: BMP signaling in craniofacial development. *Cytokine Growth Factor Rev.* **27**, 129–139 (2016).
59. Dyson, H. J. & Wright, P. E. Intrinsically unstructured proteins and their functions. *Nat. Rev. Mol. Cell Biol.* **6**, 197–208 (2005).
60. Altshuler, D., Daly, M. J. & Lander, E. S. Genetic mapping in human disease. *Science* **322**, 881–888 (2008).
61. Genomes Project, C. et al. A global reference for human genetic variation. *Nature* **526**, 68–74 (2015).
62. Knowles, T. P., Vendruscolo, M. & Dobson, C. M. The amyloid state and its association with protein misfolding diseases. *Nat. Rev. Mol. Cell Biol.* **15**, 384–396 (2014).
63. Tong, X. et al. Liquid-liquid phase separation in tumor biology. *Signal Transduct. Target. Ther.* **7**, 221 (2022).
64. Vermeesch, J. R., Voet, T. & Devriendt, K. Prenatal and pre-implantation genetic diagnosis. *Nat. Rev. Genet.* **17**, 643–656 (2016).
65. Strauss, R. P. & Cassell, C. H. Critical issues in craniofacial care: quality of life, costs of care, and implications of prenatal diagnosis. *Acad. Pediatr.* **9**, 427–432 (2009).
66. Guo, S. et al. Trio cooperates with Myh9 to regulate neural crest-derived craniofacial development. *Theranostics* **11**, 4316–4334 (2021).
67. Carroll, S. H. et al. An Irf6-Esrp1/2 regulatory axis controls midface morphogenesis in vertebrates. *Development* <https://doi.org/10.1242/dev.194498> (2020).
68. Favaro, F. P. et al. A noncoding expansion in EIF4A3 causes Richieri-Costa-Pereira syndrome, a craniofacial disorder associated with limb defects. *Am. J. Hum. Genet.* **94**, 120–128 (2014).
69. Yu, Z. et al. Induction of cell-cycle arrest by all-trans retinoic acid in mouse embryonic palatal mesenchymal (MEPM) cells. *Toxicol. Sci.* **83**, 349–354 (2005).
70. Yu, K., Karuppaiah, K. & Ornitz, D. M. Mesenchymal fibroblast growth factor receptor signaling regulates palatal shelf elevation during secondary palate formation. *Dev. Dyn.* **244**, 1427–1438 (2015).
71. Almaidhan, A. et al. Neural crest-specific deletion of Ldb1 leads to cleft secondary palate with impaired palatal shelf elevation. *BMC Dev. Biol.* **14**, 3 (2014).

Acknowledgements

This work was supported by the National Natural Science Foundation of China (82170911 to M.J., 82372991 to C.L.), Key Research Program in Jiangsu Province-Social Development Project (BE2021724 to M.J.).

Author contributions

M.L., C.L., and M.J. contributed to the conception and design of the study. M.L., J.Y., and Y.J. conducted the experiments. M.L. and J.Y. performed the statistical analysis. M.L., C.Y., and C.L. provided technical assistance and supervision. M.L., G.S., and M.J. provided critical resources. M.L., J.Y., and C.L. wrote sections of the manuscript with input from all co-authors. All authors contributed to the interpretations, discussions, and conclusions presented.

Competing interests

The authors declare no competing interests.

Additional information

Supplementary information The online version contains supplementary material available at <https://doi.org/10.1038/s41467-025-56327-6>.

Correspondence and requests for materials should be addressed to Liming Chen or Junqing Ma.

Peer review information *Nature Communications* thanks Jian Xu, and the other, anonymous, reviewers for their contribution to the peer review of this work. A peer review file is available.

Reprints and permissions information is available at <http://www.nature.com/reprints>

Publisher's note Springer Nature remains neutral with regard to jurisdictional claims in published maps and institutional affiliations.

Open Access This article is licensed under a Creative Commons Attribution-NonCommercial-NoDerivatives 4.0 International License, which permits any non-commercial use, sharing, distribution and reproduction in any medium or format, as long as you give appropriate credit to the original author(s) and the source, provide a link to the Creative Commons licence, and indicate if you modified the licensed material. You do not have permission under this licence to share adapted material derived from this article or parts of it. The images or other third party material in this article are included in the article's Creative Commons licence, unless indicated otherwise in a credit line to the material. If material is not included in the article's Creative Commons licence and your intended use is not permitted by statutory regulation or exceeds the permitted use, you will need to obtain permission directly from the copyright holder. To view a copy of this licence, visit <http://creativecommons.org/licenses/by-nc-nd/4.0/>.

© The Author(s) 2025